ELSEVIER

Contents lists available at ScienceDirect

#### Acta Materialia

journal homepage: www.elsevier.com/locate/actamat



#### Full length article

### 3D in-situ characterization of dislocation density in nickel-titanium shape memory alloys using high-energy diffraction microscopy

Wenxi Li <sup>a,b</sup>, Sangwon Lee <sup>a</sup>, Tianchi Zhang <sup>c</sup>, Yuefeng Jin <sup>a</sup>, Darren Pagan <sup>d</sup>, Lee Casalena <sup>e</sup>, Michael Mills <sup>f</sup>, Ashley Bucsek <sup>a,b,\*</sup>

- <sup>a</sup> Department of Mechanical Engineering, University of Michigan, Ann Arbor, MI 48109, USA
- <sup>b</sup> Department of Materials Science and Engineering, University of Michigan, Ann Arbor, MI 48109, USA
- <sup>c</sup> Department of Electrical Engineering and Computer Science, University of Michigan, Ann Arbor, MI 48109, USA
- d Department of Materials Science and Engineering, The Pennsylvania State University, University Park, PA 16802, USA
- e Thermo Fisher Scientific, Hillsboro OR, 97124, USA
- f Department of Materials Science and Engineering, The Ohio State University, Columbus, OH 43212, USA

#### ARTICLE INFO

# Keywords: Functional fatigue Shape memory alloy Geometrically necessary dislocation Intragranular misorientation

#### ABSTRACT:

Functional fatigue—changes to the material response during cyclic loading—is a major barrier to the cycle lifetime demands of shape memory alloy technologies. Functional fatigue is caused by permanent changes to the microstructure such as the generation of dislocations during the forward and reverse martensitic phase transformation. In this work, far-field and near-field high-energy diffraction microscopy (ff- and nf-HEDM) are used to characterize the local accumulation of geometrically necessary dislocation (GND) density in the austenite phase in situ and in 3D across a bulk Ni<sub>49,9</sub>Ti<sub>50,1</sub> polycrystalline shape memory alloy during load-biased thermal cycling. A custom nf-HEDM data analysis procedure is used to reconstruct spatially-resolved intragranular misorientation maps that are then converted to spatially-resolved GND density maps. In this way, GND density is tracked in individual grains across cycles. We find that neither Schmid factor nor the maximum transformation work correlates strongly with GND density evolution during load-biased thermal cycling. The results show that the spatially-resolved GND density is distributed heterogeneously, but GND density increases faster near grain boundaries, in grains at the sample surface, and in grains with large volumes, indicating that these regions/types of grains will undergo different functional fatigue behaviors. Finally, the effect of grain neighborhood and grain boundaries on GND evolution are investigated, highlighting the role played by grain boundaries and the grain neighborhood in the evolution of GND density. This work demonstrates the utility of nf-HEDM for understanding the evolution of subgrain-scale plastic deformation, including materials that undergo a martensitic phase transformation.

#### 1. Introduction

Nickel-titanium (NiTi) shape memory alloys are widely used in aerospace, biomedical, and soft robotics applications due to their superelastic, shape memory, and actuation behaviors as well as biocompatibility and corrosion resistance [1–12]. The deformation mechanism behind these functional behaviors is a reversible martensitic phase transformation between a B2 cubic (austenite) phase and a B19′ monoclinic (martensite) phase [13]. The longstanding challenge associated with reversible martensitic phase transformations is that they tend to not actually be reversible in practice. That is, they exhibit

functional fatigue: changes to the material response during cyclic loading that typically diminish the material's exploitative properties. Functional fatigue stems from any permanent changes to the microstructure, including the generation and accumulation of dislocations, deformation twinning, and retained martensite [14–18]. These permanent microstructure changes occur during the forward and/or reverse martensitic phase transformation and/or plastic slip and can result in irrecoverable macroscopic strain, loss of dimensional stability, and failure of the material during cyclic loading [14,16–21]. However, there is a lack of fundamental understanding of how, where, or when these permanent defects are generated, in what amounts, and how they can be

E-mail address: abucsek@umich.edu (A. Bucsek).

<sup>\*</sup> Corresponding author.

tailored.

Based on the phenomenological description of single crystal plasticity, crystallographic slip on a specific plane is carried out by the flow of statistically stored dislocations (SSDs). Geometrically necessary dislocations (GNDs) also arise, adhering to the geometric constraints of the crystal lattice to ensure lattice compatibility as deformation occurs. As plastic deformation proceeds, both GNDs and SSDs accumulate with increasing strain. SSDs are stored by mutually trapping each other randomly [22,23]. On the other hand, GNDs, due to their non-zero Burgers vector, are associated with heightened and localized orientation gradients.

The local accumulation of dislocations and other permanent microstructure changes can be characterized using scanning and transmission electron microscopy techniques. However, in practical scenarios, it is not feasible to discern or distinguish GNDs and SSDs, or to identify the transition of specific SSDs to GNDs and vice versa. Furthermore, discrete electron microscopic measurements are confined to surface-level deformation or, in the case of thin lamella samples, only to localized sub-surface deformation [19,24,25]. Few techniques offer the capability to spatially resolve internal defect accumulation and structural changes over large fields of view within bulk samples. Such a capability would enable a statistically-informed understanding of how the permanent microstructure changes associated with functional fatigue vary as a function of local microstructure features.

Over the past two decades, 3D in-situ synchrotron X-ray techniques such as 3D X-ray diffraction (3DXRD), high-energy diffraction microscopy (HEDM), and diffraction contrast tomography (DCT) have been used to nondestructively track the evolution of 3D microstructures across bulk, millimeter-sized sample volumes. This includes a number of noteworthy studies on shape memory alloys, including the following examples and several others. Berveiller et al. investigated the deformation behavior of four coarse ( $\sim$ 500  $\mu$ m) Cu<sub>78</sub>Al<sub>23</sub>Be<sub>3</sub> grains and found that austenite lattice rotation and sub-grain formation are reversible during stress-induced martensite transformation through 3DXRD [26]. Hachi et al. tracked 187 CuAlBe grains and highlighted the influence of the neighboring grains on the martensitic transformation evolution through 3DXRD and DCT [27]. Sedmak et al. revealed that localized martensite transformation was induced by the increase of shear stress elevation near the front interface of ~15,000 austenite grains in a NiTi wire using 3DXRD [28]. Paranjape et al. found the stress redistribution of austenite and martensite phases in a NiTi single crystal during phase transformation and inclusions could influence the activation of martensite variants through far-field HEDM (ff-HEDM) and numerical simulation [29], and also studied the grain-averaged response of individual grains in polycrystalline NiTi during stress-induced transformation and discussed the granular constraint and surface effects of heterogeneous grain response [30]. Bucsek et al. discussed the difference between prediction of martensite evolution using crystallographic theory of martensite and ff-HEDM experiment results in a NiTi sample using a forward model approach [31], revealed the evolution of stress-induced monoclinic twin microstructures and the sequence of twin rearrangement mechanisms on the basis of HEDM data [32], and studied the emergence of  $\Sigma 3$  and  $\Sigma 9$ -type grain boundaries in a single NiTi crystal subjected to load-biased thermal cycling using nf-HEDM

While these works show the individual grain responses of shape memory alloys under different loading conditions, the local (i.e., intragranular) lattice distortion and dislocation accumulation within individual grains are not typically captured using conventional 3DXRD, HEDM, or DCT. Of particular usefulness would be the ability to measure intragranular misorientation, as it can be used to quantify the local degree of plastic deformation [34–37]. Moreover, regions of large reorientation are typically connected to regions of high stress and plastic strain and are likely future sites of catastrophic events like crack initiation. Hence, the ability to track the evolution of intragranular misorientation can improve our ability to understand crystal plasticity, fatigue,

and failure in shape memory alloys, and in crystalline materials in general [38–41].

The software package developed by Suter et al. [42] now known as HEXOMAP [43] can analyze intragranular misorientation from nf-HEDM data collected with a line-focused beam, but the reconstruction approach utilizes a blend of discrete orientation space search and Monte Carlo optimization, which is different than the crystallographic orientation fiber approach implemented in the HEXRD software [44,45] and in the present work. In addition to the work by Bucsek et al. [33] and others, Nygren et al. recently demonstrated a reconstruction procedure for spatially resolving intragranular misorientation using a "box" beam in HEDM measurements (allowing for more grains/voxels to by characterized simultaneously) using the latter approach [46]. Instead of measuring the grain-averaged crystallographic orientation of each grain, Nygren et al. showed how it is possible to extract the local intragranular misorientation from combined nf-HEDM and ff-HEDM data sets. Inspired by these works, we use a similar approach to spatially resolve the intragranular misorientation across a bulk polycrystalline NiTi shape memory alloy during load-biased thermal cycling (replicating shape memory alloy actuation application environments) [16,25]. 3D maps of intragranular misorientation are measured in the austenite phase pre-loading (cycle 0) and after 2, 5, 10, and 20 cycles. These 3D maps of intragranular misorientation are then used to estimate lower bounds of GND density (as opposed to randomly distributed and mutually trapped SSD density that do not contribute to the lattice curvature). By comparing the GND density maps to the spatially-resolved orientation maps, we are able to quantify the evolution of GND density for each individual grain and search for statistical correlations between GND density accumulation and different microstructure features.

#### 2. Materials and methods

#### 2.1. Sample preparation and HEDM experiments

A hot-extruded, hot-straightened polycrystalline Ni<sub>49.9</sub>Ti<sub>50.1</sub> (at.%) rod with a diameter of 10 mm was prepared by Nitinol Devices and Components. After solutionizing treatments for 30 min at 900 °C followed by water quenching, the grains had an average size of 75  $\mu m$ . The sample was electrical-discharge-machined into a dog-bone tensile specimen with a 1  $\times$  1  $\times$  1  $\text{mm}^3$  gage section. The transformation temperature measured by differential scanning calorimetry was  $M_{\rm f} = 71\,$  $^{\circ}\text{C}\text{, }M_{s}=55~^{\circ}\text{C}\text{, }A_{s}=84~^{\circ}\text{C}$  and  $A_{f}=97~^{\circ}\text{C}\text{.}$  Ff-HEDM and nf-HEDM experiments were performed at the F2 beamline at the Cornell High Energy Synchrotron Source (CHESS). The mechanical loading was applied by the second generation rotational and axial motion system (RAMS2) developed by the Air Force Research Laboratory [47]. An X-ray beam size of 120  $\mu m$  (height)  $\times$  2.5 mm (width) with an energy of 55.618 keV was used to illuminate the sample at the center of the gauge section. CeO2 and gold standards were used to calibrate the detector translations, tilts, and distortion. The ff-HEDM measurements were taken on a General Electric (GE) flat-panel area detector with  $2048 \times 2048$  pixels and  $200 \times 200$   $\mu m^2$  pixel sizes placed 1045.7 mm downstream of the sample. The sample was rotated  $360^{\circ}$  about the vertical rotation axis (also the loading direction), and ff-HEDM images were collected every 0.25° with an exposure time of 0.25 s per image. The nf-HEDM measurements were taken on a Retiga 4000 DC detector with an infinity optical system and Mitutoyo objectives with 1.48×1.48 μm<sup>2</sup> per pixel placed 12.91 mm downstream of the sample. The nf-HEDM diffraction images were taken every 0.25° with an exposure time of 5 s per image.

The initial measurement was taken at 120  $^{\circ}\text{C} \pm 5 \,^{\circ}\text{C}$  without mechanical loading (referred to as cycle 0). Then, a tensile bias load of 150 MPa was applied to the sample and held constant for the remainder of the experiment. During each cycle, the sample was cooled to 20  $^{\circ}\text{C}$  and heated back to 120  $^{\circ}\text{C}$ . The temperature was applied by a custom-built, dual halogen bulb line focusing furnace. Argon was continuously

flowing through the chamber during the testing to minimize the oxidation effects. Ff-HEDM and nf-HEDM measurements were taken at cycles 0, 2, 5, 10, and 20 at 120  $^{\circ}\text{C}$  (i.e., all measurements were taken when the sample was in the austenite phase).

#### 2.2. Intragranular misorientation analysis procedure

Fig. S1 shows what the nf-HEDM diffraction images look like before and after cycling. The rectangle at the center of the images is the transmitted beam, and the other "spots" are Bragg reflections. The appearance of the Bragg reflections before versus after cycling provides insights into the microstructural changes that occur as a result of cycling. Initially (cycle 0), the Bragg reflections have relatively sharp edges (Fig. S1(a)). However, as the fatigue test progresses to cycle 20, the Bragg reflections gradually lose their sharpness, spreading especially along the azimuthal direction (Fig. S1(b)). These changes are signatures of changes in the intragranular misorientation caused by the plastic deformation of the NiTi sample. The smearing of the Bragg reflections and the decrease in their sharpness also pose challenges for conventional HEDM reconstruction processes. As a result, we required a specialized analysis routine to extract the underlying intragranular misorientation evolution, as described below.

The software package HEXRD [44,45] was used to analyze the ff- and nf-HEDM data and for the intragranular misorientation analysis. The results are then compiled and visualized utilizing the open-source software package Paraview [48]. An overview of 3D intragranular misorientation reconstruction for one individual grain is presented in Fig. 1. The procedure is as follows. First, the conventional ff-HEDM analysis is performed to obtain a list of grain-averaged orientations for each grain in the diffraction volume via peak indexing and parameter refinement process. Second, the conventional nf-HEDM analysis is performed to voxelate the diffraction volume and assign each voxel to one of the grain-averaged orientations using forward modeling, or virtual

diffraction [49]. The voxel size used here was 5  $\mu m$  horizontal and 10  $\mu m$  vertical. (The larger vertical voxel dimension was chosen to reduce computation time.) The results of these two steps are shown in Fig. 1(a): a 3D spatially-resolved orientation map assuming a single orientation within each grain. The details associated with determining these grain-averaged quantities from ff-HEDM and nf-HEDM are provided in [42,50].

Next, a modified ff-HEDM algorithm is used to obtain the orientation envelope for each grain. This process is shown in Fig. 1(b–e). The grain-averaged orientations of all the grains are plotted in orientation space in Fig. 1(b). For each grain, its grain-averaged orientation is selected, and a list of trial orientations with an angular spread of  $\pm$  5° and a spacing of 0.25° along each direction in Rodrigues space is discretized around the grain-averaged orientation in the 3D orientation space. This is shown in Fig. 1(c,d). Virtual diffraction is then performed using each trial orientation for each voxel. Of these trial orientations, all orientations with a completeness value (the number of measured Bragg reflections divided by the number of expected Bragg reflections) above a prescribed threshold (we used 0.8 here) are stored, and the orientation with the highest completeness value above 0.8 is assigned to the voxel. The result, the full orientation envelope for each grain, is shown in Fig. 1(e).

The virtual diffraction of each trial orientation at each voxel and the assignment of the highest completeness orientation to each voxel are shown in Fig. 1(f-h). First, the voxels associated with one particular grain are identified and dilated by two voxels as shown in Fig. 1(f). (The dilation is to account for a potential improvement in the grain reconstruction near the grain boundaries following the intragranular misorientation reconstruction, or for small changes in grain structure during deformation as suggested by Nygren et al. in [46].) For each voxel in the dilated grain volume, virtual diffraction is performed using each "spread" trial orientation for this particular grain as shown in Fig. 1(d). The orientation with the highest completeness value is assigned to this voxel. These steps are repeated for each grain. Due to the dilation

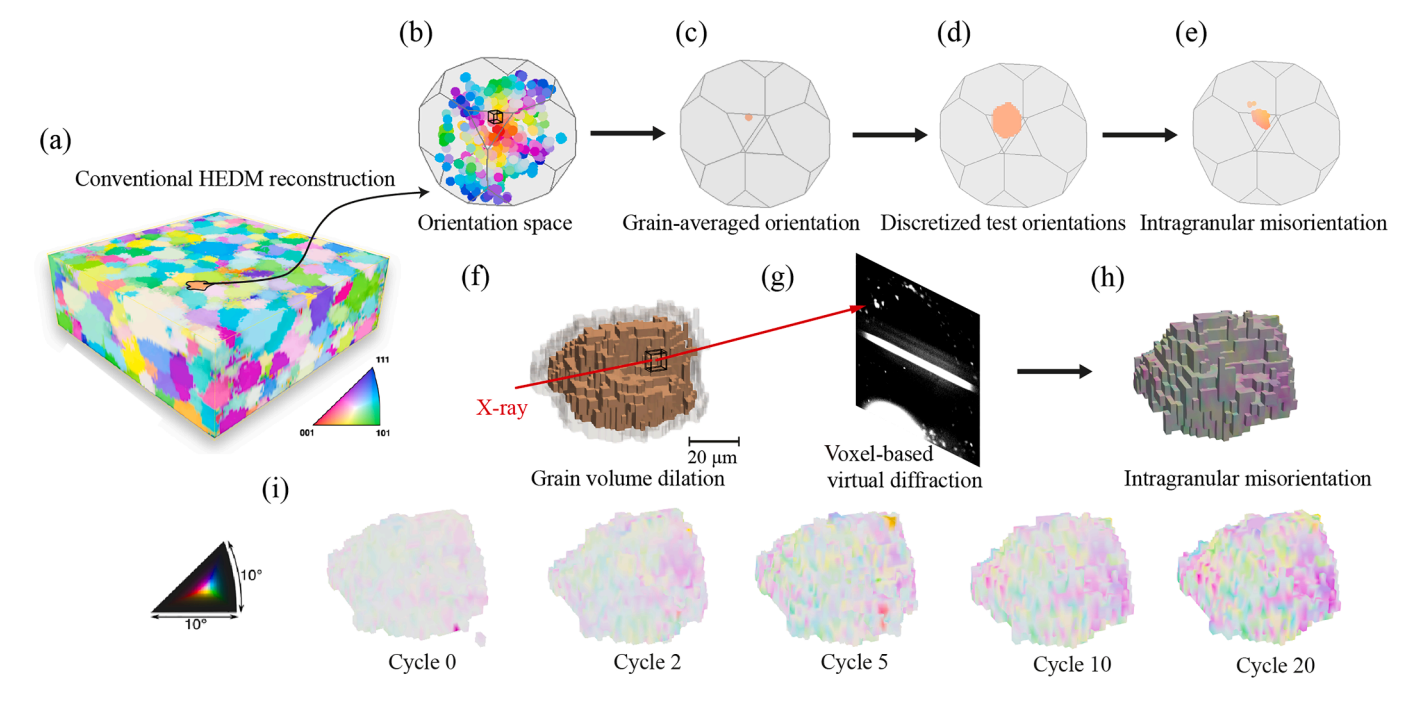


Fig. 1. Flowchart of the intragranular misorientation reconstruction procedure using ff-HEDM and nf-HEDM. First, the spatially-resolved grain-averaged orientation map is obtained from the conventional HEDM analysis (a). (IPF direction parallel to the loading axis.) Then, from all of the grain-averaged orientations shown in (b), one grain-averaged orientation is selected at a time (c), then spread and discretized into new trial orientations (d). These trial orientations are tested using a modified ff-HEDM analysis, resulting in an orientation envelope representing the intragranular misorientation (e). For each individual grain, the grain volume is dilated and the grain is voxelated (f). For each voxel, virtual nf-HEDM diffraction is performed using the test orientations from (e) (g), resulting in the intragranular misorientation reconstruction of each grain (h). An example of grain reconstruction result is shown across different cycles in (i), using a stretched IPF color map to highlight the intragranular misorientation. (For interpretation of the references to color in this figure legend, the reader is referred to the web version of this article.)

operation and independent reconstruction of each grain, voxels that are close to the grain boundaries will be assigned with multiple orientations. When all the grains are assembled back into the volume, the overlapping voxels are assigned to the orientation with the highest completeness value. An example of the intragranular misorientation reconstruction is shown for one individual grain in Fig. 1 (h,i) for each actuation cycle, where the inverse pole figure (IPF) color map is stretched to  $10^{\circ}$  along each direction to highlight the intragranular misorientation.

W. Li et al.

To validate the accuracy of the intragranular misorientation reconstruction procedure, a series of tests are conducted using synthetic diffraction data from a virtual 'phantom' grain dataset. A virtual polycrystalline copper sample is deformed under tensile uniaxial loading to a strain of 10 %. From this polycrystal, a grain with an orientation spread larger than 5° is selected, and this grain and its surrounding neighborhood are used to synthesize virtual ff- and nf-HEDM diffraction images. Two different beam sizes, a 1D "line" beam and a 2D "box" beam are simulated to illuminate the layer of interest (in the line beam case) and volume of interest (in the box beam case) in the virtual sample both before and after deformation. The central layer in the four scenarios (undeformed microstructure with a line beam, undeformed microstructure with a box beam, deformed microstructure with a line beam, and deformed microstructure with a box beam) are then reconstructed using the intragranular misorientation analysis procedure described above and compared with the original microstructure inputs. The results, show that the intragranular analysis procedure presented in this work can accurately capture both grain shape and spatially-resolved

intragranular misorientation with high accuracy, even for grains with large orientation spread due to significant plastic deformation. The details are provided in Appendix A and the Supplemental Material. The results are shown in Fig. A2, Fig. A3, and Fig. A4 for the box beam and Fig. S2 and S3 for the line beam.

Fig. 2 presents a comparison of spatially-resolved completeness and intragranular misorientation results as analyzed by conventional nf-HEDM (shown in Fig. 2(a,c)) versus intragranular nf-HEDM analysis (illustrated in Fig. 2(b,d)). This comparison is for a single layer of the reconstructions at cycle 0. For the conventional nf-HEDM completeness map in Fig. 2(a), the completeness is relatively high in the grain centers but decreases near the grain boundaries, and only a single orientation is assigned to each grain; therefore, no intragranular misorientation is obtained in Fig. 2(c). The average completeness value in Fig. 2(a) is 0.66, with a minimum value of 0.33. With the intragranular nf-HEDM analysis, the completeness value is improved (relative to conventional nf-HEDM), even near the grain boundaries (Fig. 2(b)). The average completeness value in Fig. 2(b) is 0.84, with a minimum value of 0.54. Fig. 2(d) shows the resulting spatially-resolved intragranular misorientation, colored with a maximum misorientation angle of 3°.

Fig. 3 shows the reconstruction of the full  $1 \times 1 \times 0.1$  mm<sup>3</sup> diffraction volume. Fig. 3(a) shows the initial 3D grain map at cycle 0. A comparison is shown between the conventional grain-averaged (Fig. 3 (b)) and intragranular (Fig. 3(c)) reconstructions at cycle 20. As expected, the grain-averaged reconstructions show essentially no intragranular misorientation, and the intragranular reconstruction reveals

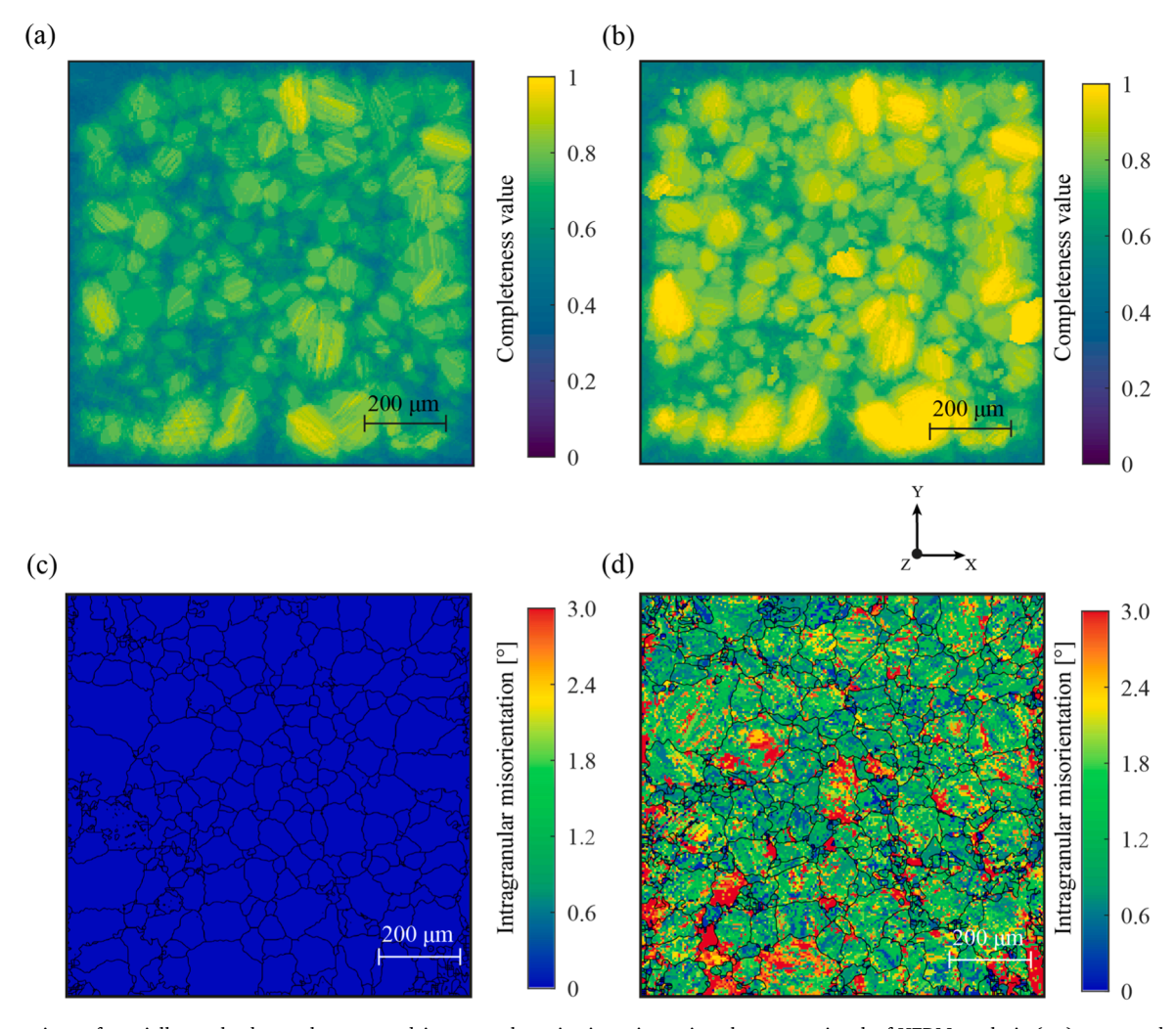


Fig. 2. Comparison of spatially-resolved completeness and intragranular misorientation using the conventional nf-HEDM analysis (a,c) compared against the intragranular nf-HEDM analysis (b,d) for a single layer of the reconstructions for cycle 0. Z is the loading direction.

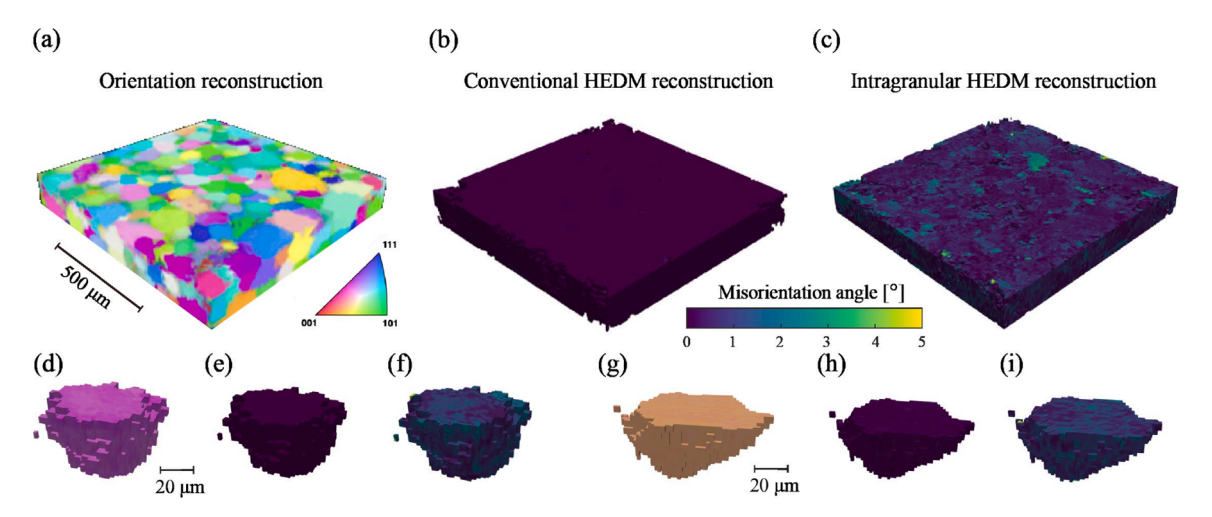


Fig. 3. 3D grain map of the diffracted volume showing the grain-averaged orientations at cycle 0 (a) (IPF direction parallel to the loading axis). Comparison of spatially-resolved intragranular misorientation using the conventional nf-HEDM analysis (b) against the intragranular nf-HEDM analysis (c) for cycle 20. Comparison of spatially-resolved orientation (d,g) and intragranular misorientation (e,f,h,i) using the conventional nf-HEDM analysis (e,h) against the intragranular nf-HEDM analysis (f,i) for cycle 20.

the substantial intragranular misorientation across the 3D volume. Fig. 3 (d–f) and Fig. 3(g–i) show two examples of individual grains, again comparing the conventional grain-averaged against the intragranular analysis results. The new intragranular misorientation reveals the heterogeneous, grain-specific evolution of intragranular misorientation with cycling.

#### 2.3. GND density calculation procedure

For the calculation of GND density maps, we utilized the MATLAB toolbox MTEX 5.8.1 that is based on the approach proposed by Pantleon [51]. These maps are calculated from the measured spatially-resolved intragranular misorientation, assuming that the misorientation arises from GNDs with excess Burgers vector accumulated during heterogeneous inelastic deformation (in this case slip and martensitic phase transformation). From the misorientation (orientation difference) between two neighboring voxels, the curvature tensor between two measured voxels can be calculated. Then, the dislocation density tensor that characterizes the deformed state (lattice rotation and elastic strain) can be calculated from the curvature tensor, as proposed by Nye [22], neglecting the elastic strain contribution [36,51-53]. (Recent studies have shown the elastic strain contribution is insignificant compared to the lattice rotation from HR-EBSD experiments [54,55].) With 2D maps of intragranular misorientation (e.g., Fig. 2), six components of the curvature tensor and five of the nine dislocation density tensor components can be calculated. The total dislocation density tensor is a sum over the dislocation density contributions from each dislocation type. In a typical crystal, the number of dislocation types is greater than the number of obtained dislocation tensor components, which renders the linear system of fitting individual dislocation densities to dislocation density tensor components underdetermined [51,53-55]. As a result, there is no unique solution, but Pantleon [51] proposed the determination of a lower bound for the total dislocation density by minimizing the total line energy [51,52] based on the assumption that the dislocations are in a low elastic energy configuration. This is the approach used by the MATLAB toolbox MTEX 5.8.1 [56] and here.

In this study, prior to calculating the maps of GND density, a half-quadratic filter is firstly applied to denoise the HEDM intragranular misorientation data [57]. Then, the Kernel average misorientation (KAM), i.e., the average misorientation around a measurement point with respect to its nearest neighbor point, at each voxel is calculated. The order of nearest neighbor is 2 in this work, and any contributions to KAM that exceed  $5^{\circ}$  are excluded assuming that they correspond to a

neighboring grain. By neglecting the elastic strain contribution, five of the nine dislocation tensor components are calculated from intragranular nf-HEDM analysis and additionally, the difference between two components  $(\alpha_{11} - \alpha_{22})$  is used as a further constraint to improve the accuracy of estimating the GND density as proposed by Pantleon [51]. In case of  $Ni_{49.9}Ti_{50.1}$  shape memory alloys, the {110}<100> and {010}< 100>[58-60] slip systems are considered as dominant, with 24 possible edge dislocation and 6 possible screw dislocation configurations. By using energy minimization as explained above, the lower bounds of the total GND densities can be estimated. Finally, 3D maps of spatially-resolved GND density are obtained by stitching the 2D GND maps along the vertical direction. Due to lower reconstruction resolution used for the vertical (layer-stitching) direction (10  $\mu m$  vs. 5  $\mu m$  horizontally), the orientation gradient along the vertical direction is not considered in this paper. Including the misorientation across all three dimensions is a future extension of this work.

#### 2.4. Grain tracking algorithm

Since the intragranular misorientation reconstruction algorithm assigns a unique orientation to each voxel, we can identify all of the voxels belonging to a single grain by grouping sets of connected voxels with similar orientations, and separating its neighbor voxels with orientation discontinuities. Because the grain locations can shift during loading, this grain identification procedure must be repeated for each measurement and then grains must be assigned to same grains across different measurements. Fig. 4 shows an example of our grain tracking process. First, the list of voxels belonging to each grain is assigned for each measurement. Then, for each grain in cycle 0 (e.g., for the grain shown in Fig. 4 (a,c) that is arbitrarily called grain 97, the same grain must be identified in all of the other cycles. To do so, we assumed that each grain would not rotate (on average) more than 5°, and its centroid would not drift more than 50 µm. Fig. 4(b) shows all of the candidate grains in cycle 20 that are approximately located where grain 97 was in cycle 0, but only one of these grains (grain 88 shown in Fig. 4(d)) fits both the location and rotation criteria. A final visual comparison of Fig. 4(c,d) confirms that the two grains are identical in the deformed state. While the numbers and assignments of voxels may change slightly for each measurement, the grain morphology stays the same.

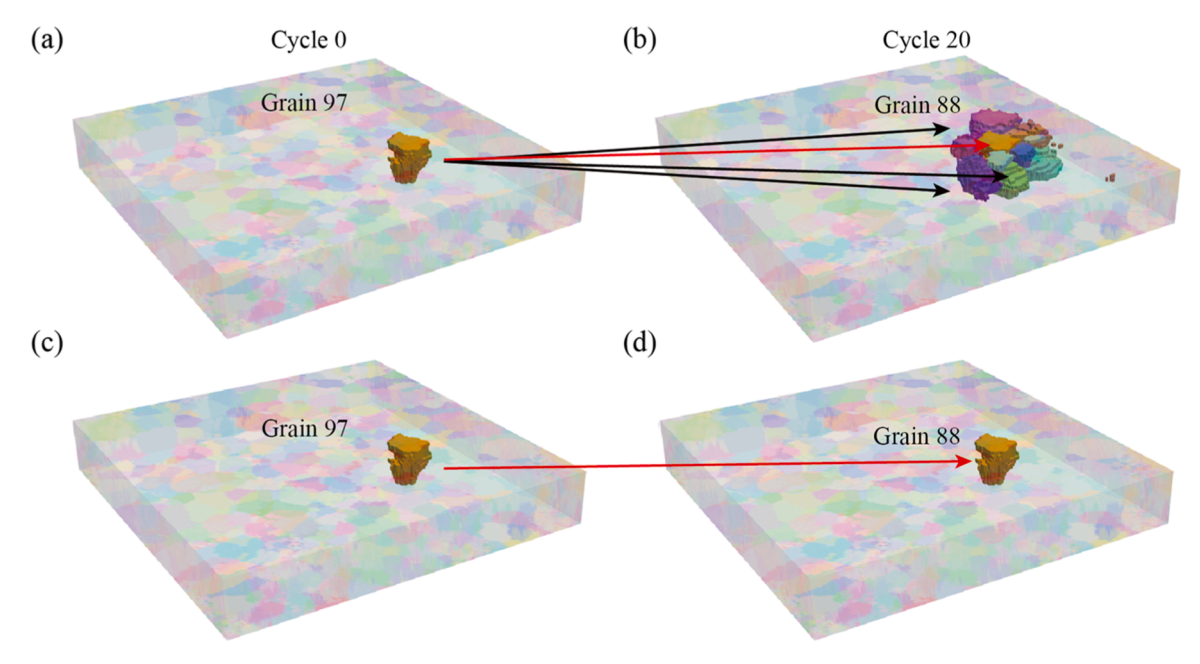


Fig. 4. Demonstration of grain tracking algorithm. For one specific grain (e.g., grain 97) in cycle 0 (a), the potential candidates for the same grain in cycle 20 are identified as those having centroids within 50  $\mu$ m of that of grain 97 (b). However, after enforcing the additional requirement that the average orientation cannot change by more than 5°, the correct grain is identified (c,d).

#### 3. Results and discussion

## 3.1. The orientation and plastic deformation evolution of individual grains

A summary of the grains identified, tracked across actuation cycles, and included in our statistical analyses is shown in Fig. 5. Only grains that contained at least 80 voxels (spherical equivalent diameter  $\sim\!35\,\mu m$ ) and retained at least 80 % of their initial volume were included. Using this selection criteria, we focused on 120 grains for our analysis. Using a spherical equivalent diameter computed from the grain volume, these 120 grains have equivalent diameters from 40–160  $\mu m$  with an average of 90  $\mu m$  and a standard deviation of 24.2  $\mu m$  (Fig. 5(a)).

To illustrate the variability of GND density accumulation for different grains, the GND density evolution for six randomly selected grains sampled over the orientation space are plotted in Fig. 5(b). For grain 1, the GND density initially increases slightly between cycles 0 and 2 and then increases more sharply between cycles 2 and 20. In contrast, for grain 2, the GND density increases steeply between cycles 0 and 2, saturates, and then increases steeply again between cycles 10 and 20. For both grains 3 and 6, the GND density increase continuously between cycles 0 and 5, slowing down between cycles 5 and 20. Finally, both grains 4 and 5 increase continuously between cycles 0 and 20. In Fig. 5 (c), the grain-averaged orientation and its rotation path are shown. The rotation in each inset figure all within 2°. Grains 1, 2, and 6 rotate continuously between cycles 0 and 20. Grain 3 and 5 rotates slightly between cycles 0 and 10 but then rotate sharply between cycles 10 and 20. Grain 4 displays a zig-zag rotation path. In Fig. 5(d), the orientation spread and the mean orientation at cycle 0 and cycle 20 are shown. The orientations are distributed heterogeneously around the mean orientations, and the orientations are much more spread in cycle 20 versus cycle 0. For all of these measures—i.e., GND density accumulation, rotation, and orientation spread—, the results illustrate a spatially heterogeneous plastic deformation of the grain-scale microstructure that occurs during cycling.

To visualize the local 3D microstructure evolution, Fig. 6(a) shows the 3D spatially-resolved maps of GND density evolution of the entire diffracted volume at each cycle. In the initial solution treated microstructure (cycle 0), the GND density is relatively low, and GND density

can be seen increasing heterogeneously across the microstructure as early as cycle 2 (the first load step measured after the initial microstructure). Fig. 6(b) shows the 3D spatially-resolved maps of GND density evolution for the six example grains from Fig. 5 at each cycle. In most grains, the GND density can be seen accumulating over the entire grain and slightly faster near grain boundaries (although observations near grain boundaries should be interpreted with care due to low completeness, since the reconstruction completeness decreases near grain boundaries; see Fig. 2). Yet, each grain's GND density evolution is different (as was also discussed for Fig. 5). Together, Figs. 5 and 6 demonstrate that the spatial distribution and the degree of plastic deformation are different for each grain, as is when each grain plastically deforms (i.e., between which cycles). These differences are likely the result of several factors, potentially including grain orientation, grain size, grain morphology, and constraints from grain neighborhoods. In the following sections, we investigate whether or not these microstructural features show any significant statistical correlation with the grains' cyclic evolution of GND density.

#### 3.2. Effect of the grain orientation on plastic deformation

In Fig. 7, we explore the existence of a correlation between grain orientation and the cyclic evolution of GND density. Fig 7(a) shows the increase in GND density between cycles 0 and 20 as a function of the initial grain-averaged orientation. Each marker represents a grain, the marker color represents the magnitude of the increase in GND density between cycles 0 and 20, and marker size represents the grain's relative volume at cycle 0. Fig. 7(b) shows the grain rotation magnitude and rotation path direction as a function of the initial grain-averaged orientation. For both Fig. 7(a) and (b), there is no strong correlation between the initial grain orientation and either the accumulation of GND density or grain rotation. That means two grains with similar orientations will not necessarily follow the same rotation path or GND density accumulation behavior.

The lack of correlation between grain orientation and plastic deformation shown in Fig. 7(a) and (b) is somewhat surprising, because we commonly assume that plastic slip and martensitic phase transformation are dependent on a grain's orientation with respect to the loading direction. The expected relationship between orientation, plastic slip, and

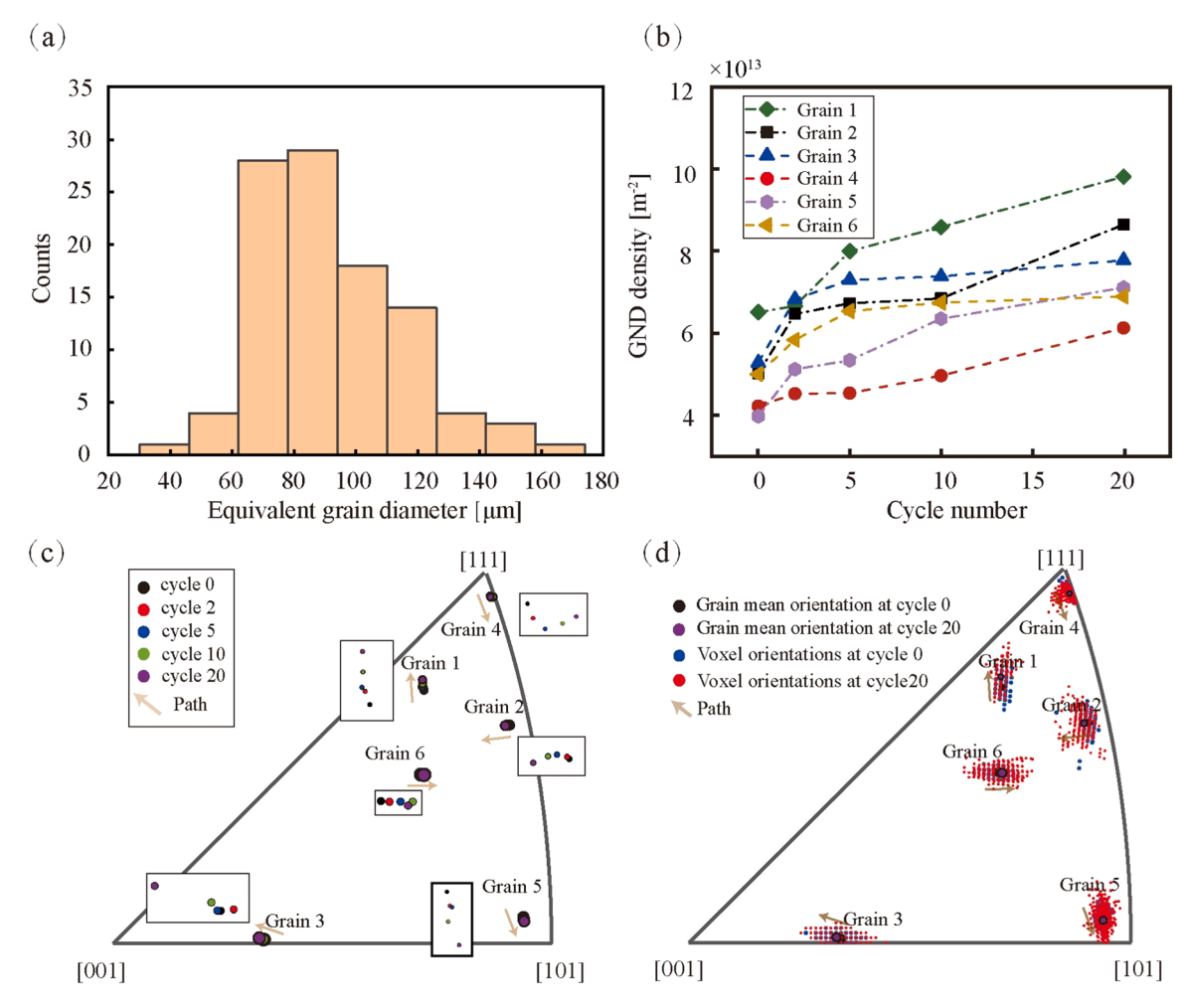
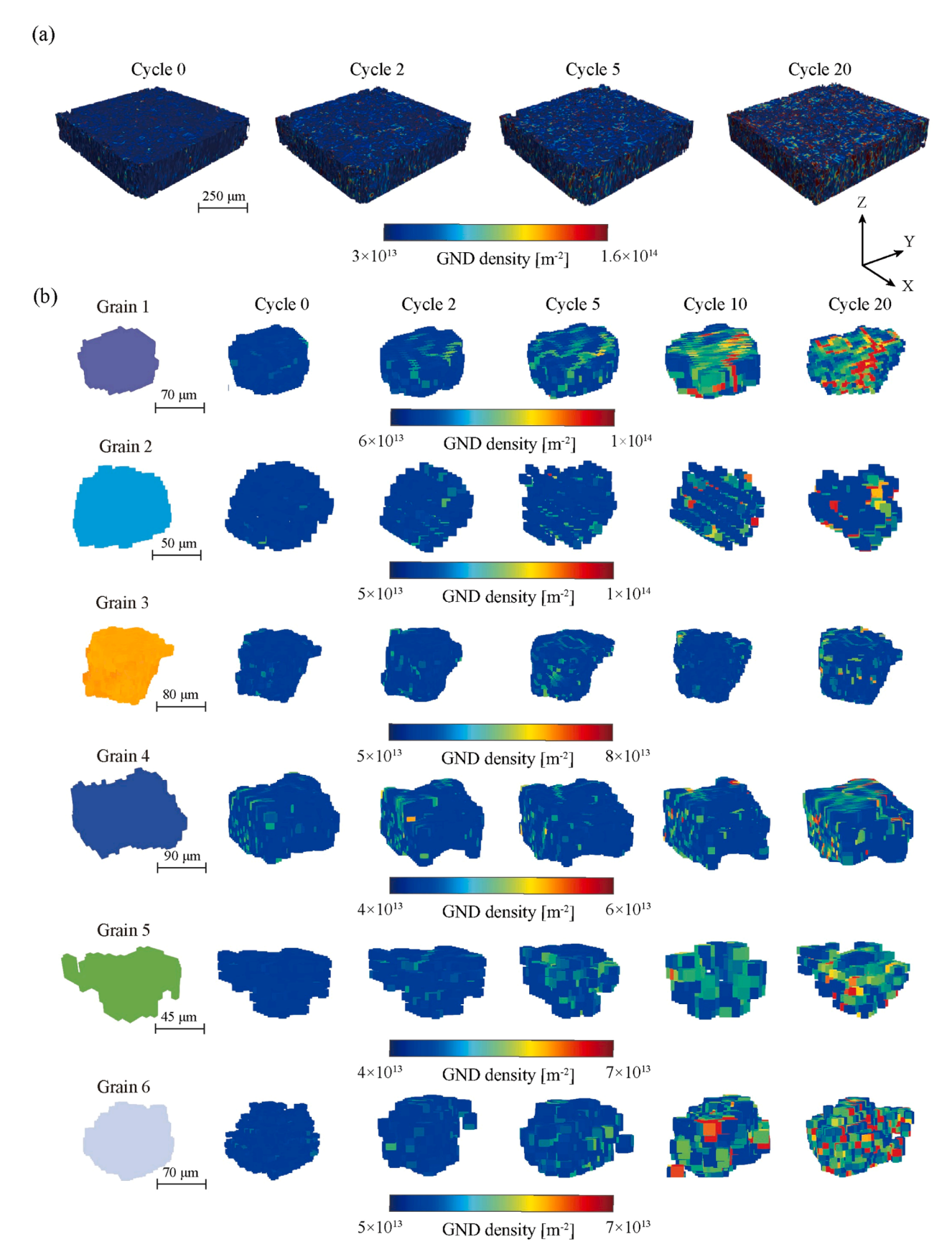


Fig. 5. The grain size for the 120 grains selected for the analysis at cycle 0 (a). The evolution of total GND density between cycles 0 and 20 for six selected grains (b). The rotation of these six grains between cycles 0 and 20 (c). The orientation spread of these six grains around the mean orientation between cycles 0 and 20 (d). The brown arrows represent the grain rotation path.

the accumulation of GND density is summarized in Schmid's law: the most popular criterion for plastic slip (likelihood and preferential slip system). Schmid's law says that grains with large Schmid factors are the most likely to undergo plastic slip, which we would expect to then cause large GND density accumulation. The expected relationship between orientation, martensitic phase transformation behavior, and the accumulation of GND density is more nuanced and less understood. Using scanning transmission electron microscopy (STEM), Bowers et al. showed that load-biased thermal loading resulted in the formation of preferential martensite habit plane variants [25]. Intuitively, we would expect that the formation of preferential martensite habit plane variants may be important for understanding GND density accumulation, because: First, each martensite habit plane variant is expected to have different interfacial stress fields (dependent on the degree of kinematic compatibility, e.g., [61,62]); Second, these interfacial stress fields presumably govern the activation of dislocations during the martensitic phase transformation. In the next paragraph, we investigate whether there is a relationship between orientation and the accumulation of GND density by way of a criterion for habit plane variant selection. There are two different criteria for predicting the preferential habit plane variant: the maximum resolved shear stress criterion [63-65] and the maximum transformation work criterion [65,66]. Here, we use the maximum transformation work criterion, which has been shown to be more accurate (e.g., [66]). Specifically, we use the calculation procedure published in [31], where the values are normalized by the magnitude of the macroscopic stress (see Eq. 13 in [31]).

To further investigate whether there is a correlation between grain orientation and plastic deformation, Fig. 7(c) shows the increase in GND density between cycles 0 and 20 as a function of Schmid factor for plastic slip, and Fig. 7(d) shows the increase in GND density between cycles 0 and 20 as a function the maximum transformation work. The Schmid factor is calculated using the initial grain orientation and the two common NiTi slip systems {110}<100> and {010}<100>. The maximum transformation work is calculated according to the procedure described in [31]. Again, the results show no strong correlation between GND density accumulation with either Schmid factor (Fig. 7(c)) or maximum transformation work (Fig. 7(d)). The only relationship that we can decipher is that the spread in GND density increase appears to increase for grains that are likely to slip (i.e., have large Schmid factors) and/or transform (i.e., have large maximum transformation work).

To summarize the findings discussed in this section: Two grains with the same orientations may exhibit very different GND density evolutions. The finding that grain orientation does not have a significant relationship with the accumulation of GND density during load-biased thermal cycling is reminiscent of a larger movement to acknowledge the shortcomings of our ability to predict (or understand) the micromechanical behavior of polycrystalline materials. For example, in studies of plastic slip and deformation twinning in hexagonal closepacked (hcp) metals, observations showing a departure from Schmid's law are not the exception but the norm (e.g., [67–69]). Another example includes the work of Bucsek et al. [31], where they showed that the maximum work criterion fails to select the habit plane variant that forms



**Fig. 6.** 3D spatially-resolved maps of GND density at different cycles. 3D GND density evolution of reconstructed microstructure at cycles 0, 2, 5, and 20 (a). 3D GND density evolution for six selected grains in Fig. 5 from cycle 0 to cycle 20 (b). The grain orientation is colored by its IPF color. Grains stay in the *X-Y* plane, and *Z* is the loading direction. (For interpretation of the references to color in this figure legend, the reader is referred to the web version of this article.)

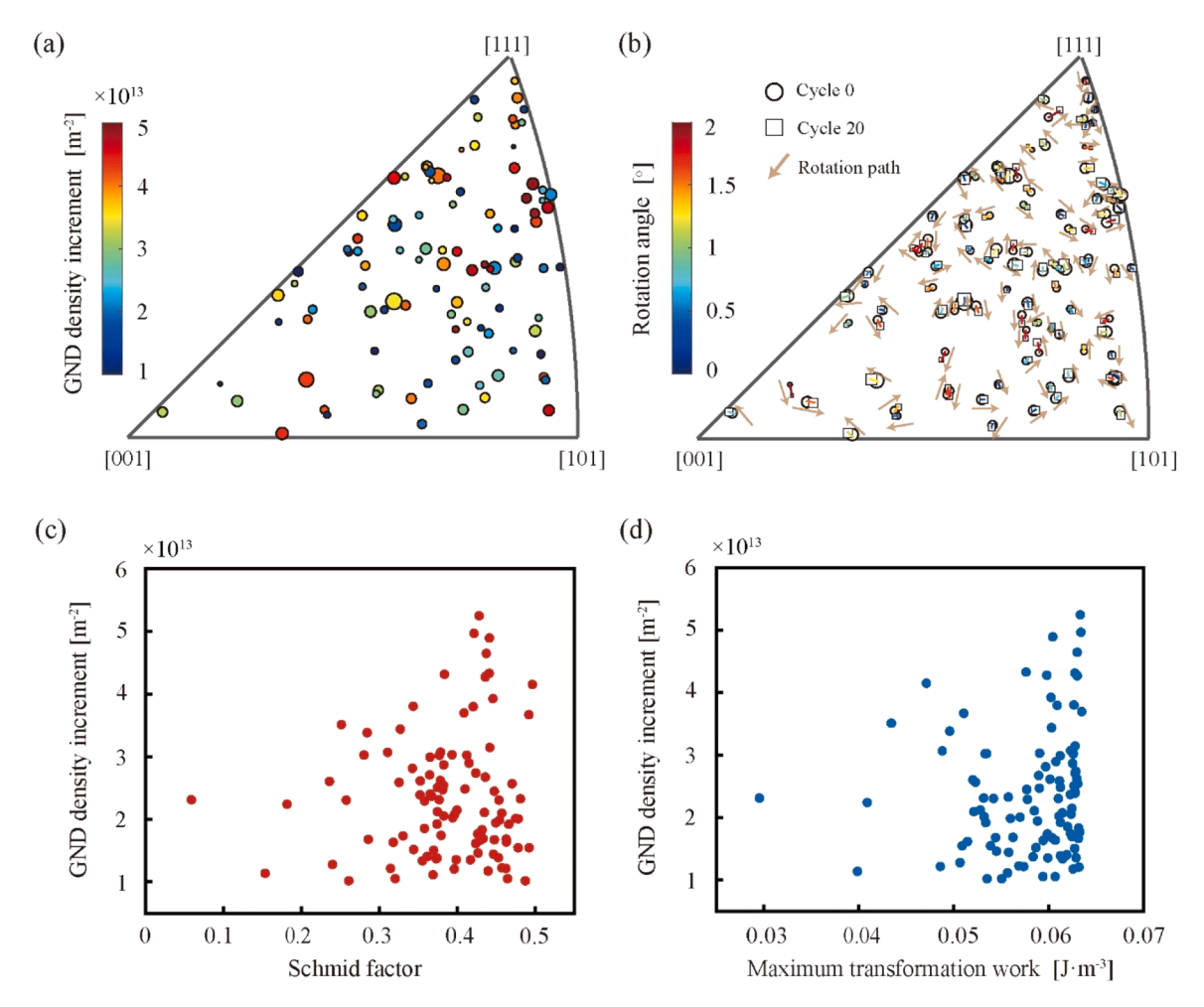


**Fig. 7.** The increase in GND density between cycles 0 and 20 as a function of the initial grain-averaged orientation (a), where each marker represents a grain, marker color represents the increase in GND density between cycles 0 and 20, and marker size represents the grain's relative volume at cycle 0. The grain rotation magnitude and direction between cycles 0 and 20 are shown as a function of the initial grain-averaged orientation (b). (IPF direction parallel to the loading direction.) The increase in GND density versus the Schmid factor for plastic slip (c). The increase in GND density versus the maximum transformation work (J m<sup>-3</sup>) (d). (For interpretation of the references to color in this figure legend, the reader is referred to the web version of this article.)

when microstructural features such as grain boundaries, inclusions, and precipitates are present. The likely reality is that the story is much more complex than we can predict using single-crystal derived, grain-averaged information and criteria, and that local (i.e., intragranular) stress concentrations, competing inelastic deformation mechanisms, and grain interactions dominate the underlying micromechanics [70]. This is explored more in Section 3.4.

#### 3.3. Effect of proximity to the free surface and grain size on GND density

In this section, we explore whether two additional microstructure features—proximity to the free surface and grain size—show any correlation with cyclic GND density accumulation. Fig. 8 shows the increase in GND density between cycles 0 and 20 versus the distance between the grain centroid and the free surface (Fig. 8(a)) and versus the grain size (Fig. 8(b)). Fig. 8(a) shows that the accumulation of GND density is negatively correlated with a grain's proximity to the free surface, with a Pearson's R value of -0.26. In other words, grains that are close to the free surface will accumulate more GND density than bulk grains. Intuitively, this observation makes sense, since grains on the free surface are less geometrically constrained and are therefore freer to undergo inelastic deformation. Similar results were shown for martensitic phase transformation in NiTi under uniaxial loading in [30] and for plastic slip in Ti7Al and pure Ti under uniaxial loading in [71,72]. These and other

findings on the disparities between surface and bulk deformation behavior suggests that using surface scanning technique, e.g. electron backscatter diffraction or transmission electron microscopy, to represent bulk material behavior should be used with some caution.

Fig. 8(b) shows that the accumulation of GND density is positively correlated with grain size, with a Pearson's R value of 0.35. The mechanical properties of polycrystalline material are well known to be influenced by grain size with small grains being resistant to slip transfer across grain boundaries (i.e., the Hall-Petch relationship). While the result shown in Fig. 8(b) only shows a correlation without direct evidence of a causation mechanism, one possible explanation for this correlation is that larger grains accumulate more GND density because of the increased ability of inelastic deformation mechanisms (martensitic phase transformation and plastic slip) to transfer across the grain boundaries of large grains (relative to those of smaller grains).

To investigate the synergistic effect of proximity to the free surface and grain size, the results are combined in Fig. 8(c). This figure shows that a higher accumulation of GND density data points is in the bottom middle region. It seems that grains close to the free surface with a large grain size tend to accumulate more GND density than interior (bulk) grains and relatively small grains during load-biased thermal-mechanical loading. However, it should be noted that while a large portion of the grain follows the general trend, the distribution of GND density accumulation is still wide. That indicates these two factors are still not

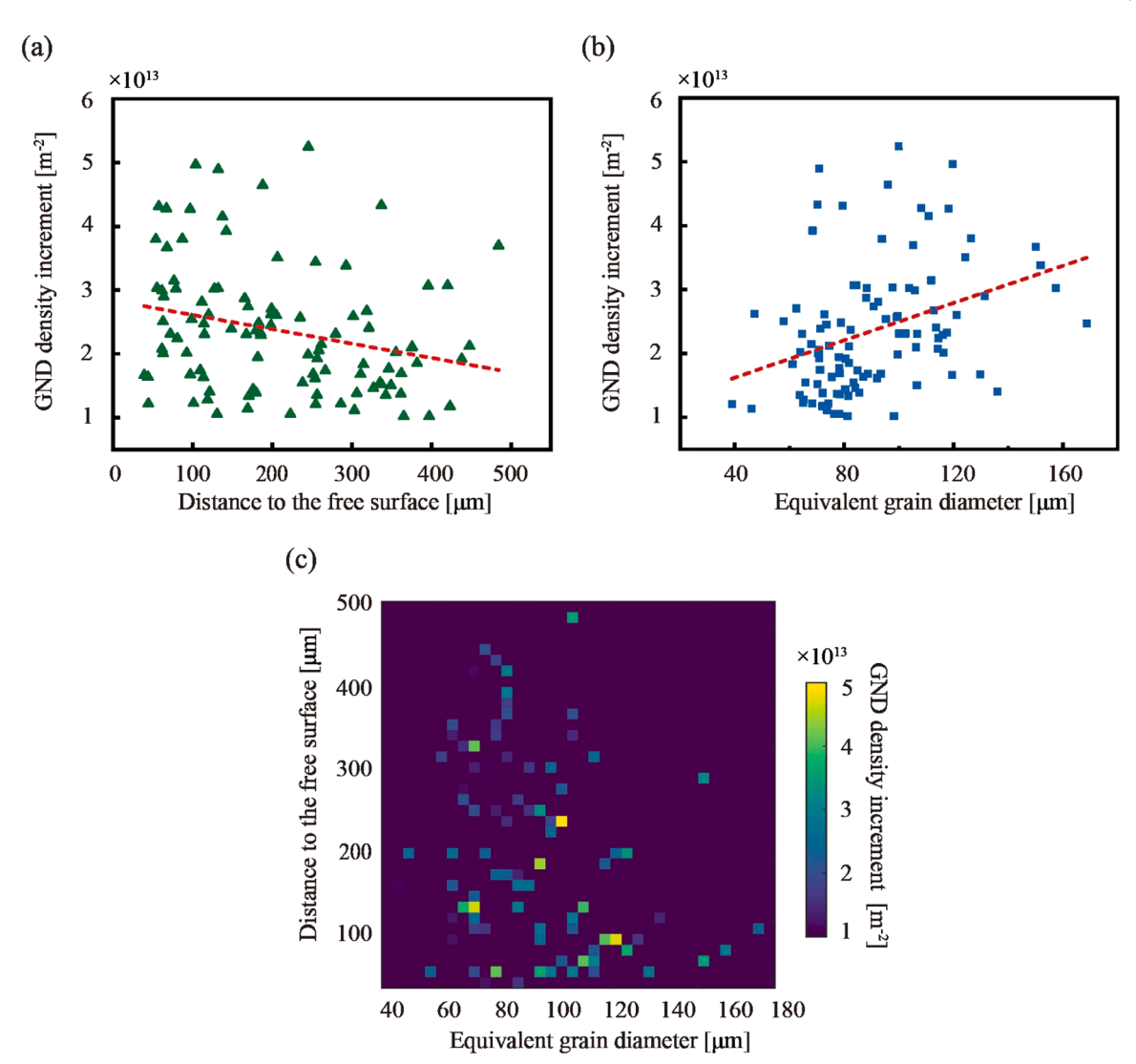


**Fig. 8.** The proximity of a grain's centroid to the closest free surface vs. the increase in GND density between cycles 0 and 20 (a) and the grain size vs. the increase in GND density between cycles 0 and 20 (b). The relationship between the grain size (*x*-axis), proximity to the free surface (*y*-axis), and increase in GND density between cycles 0 and 20 (marker size and color) (c). (For interpretation of the references to color in this figure legend, the reader is referred to the web version of this article.)

absolute indicators of GND density accumulation. Other factors should be incorporated and considered.

#### 3.4. Effect of grain neighborhood on GND density evolution

In light of the observation that grain-averaged orientation is not sufficient to predict the accumulation of GND density (Section 3.2), here, we investigate whether we can incorporate more information about the grain's surrounding neighborhood to improve our understanding. The results are presented in Fig. 9. Fig. 9(a) shows the increase in GND density between cycles 0 and 20 versus the number of grain neighbors. We use marker type and color to differentiate between surface grains and interior (bulk) grains. The results show that the increase in GND density is slightly positively correlated with the number of grain neighbors (Pearson's R value of 0.18), with no obvious difference for surface versus bulk grains.

In Fig. 9(b), we investigate the relationship between GND density accumulation and the disorientation (defined here as the minimum misorientation angle between a grain's  $<100>_{\rm B2}$  axis and the loading direction) of each grain and its neighbors (on average). Note: Grains that have  $a<100>_{\rm B2}$  axis aligned with the loading direction have the lowest Schmid factor for slip for both the  $\{011\}<100>$  and  $\{001\}<100>$  slip

systems (see, e.g., Fig. 3(b) in [73]), and they also have small transformation strains (see, e.g., Fig. 2(a) in [74]) and the lowest Schmid value for transformation (see, e.g., Fig. 2(d) in [73]). In other words, the disorientation angle combines the slip-induced and martensitic transformation-induced plasticity into a single parameter. Thus, for simplicity, we refer to close-to <100>B2 orientations as "hard" orientations, and we refer to far-from <100>B2 orientations as "soft" orientations (where "hard" means that the grain cannot easily transform or slip to induce plastic deformation). In Fig. 9(b), we observe that higher GND density accumulation occurs in the "soft" grains (high grain disorientation) versus "hard" grains (low disorientation). For example, "soft" grains with disorientation values between  $30^\circ$  and  $55^\circ$  have an average GND density accumulation of 1.5  $\times$  10<sup>13</sup> m<sup>-2</sup>, while "hard" grains with disorientation values between  $0^{\circ}$  and  $30^{\circ}$  have an average GND density accumulation of  $1.1 \times 10^{13}$  m<sup>-2</sup>. We did not observe a correlation between GND density accumulation and a grain's average grain neighbor disorientation.

While Fig. 9(b) shows no relation between GND density accumulation and the average grain neighbor disorientation, here we investigate potential effects of individual grain neighbors using two interior grains. These two grains were selected because they have nearly identical "soft" disorientation angles ( $\sim$ 40°, Fig. 9(c)), relative grain volumes (Fig. 9(e,

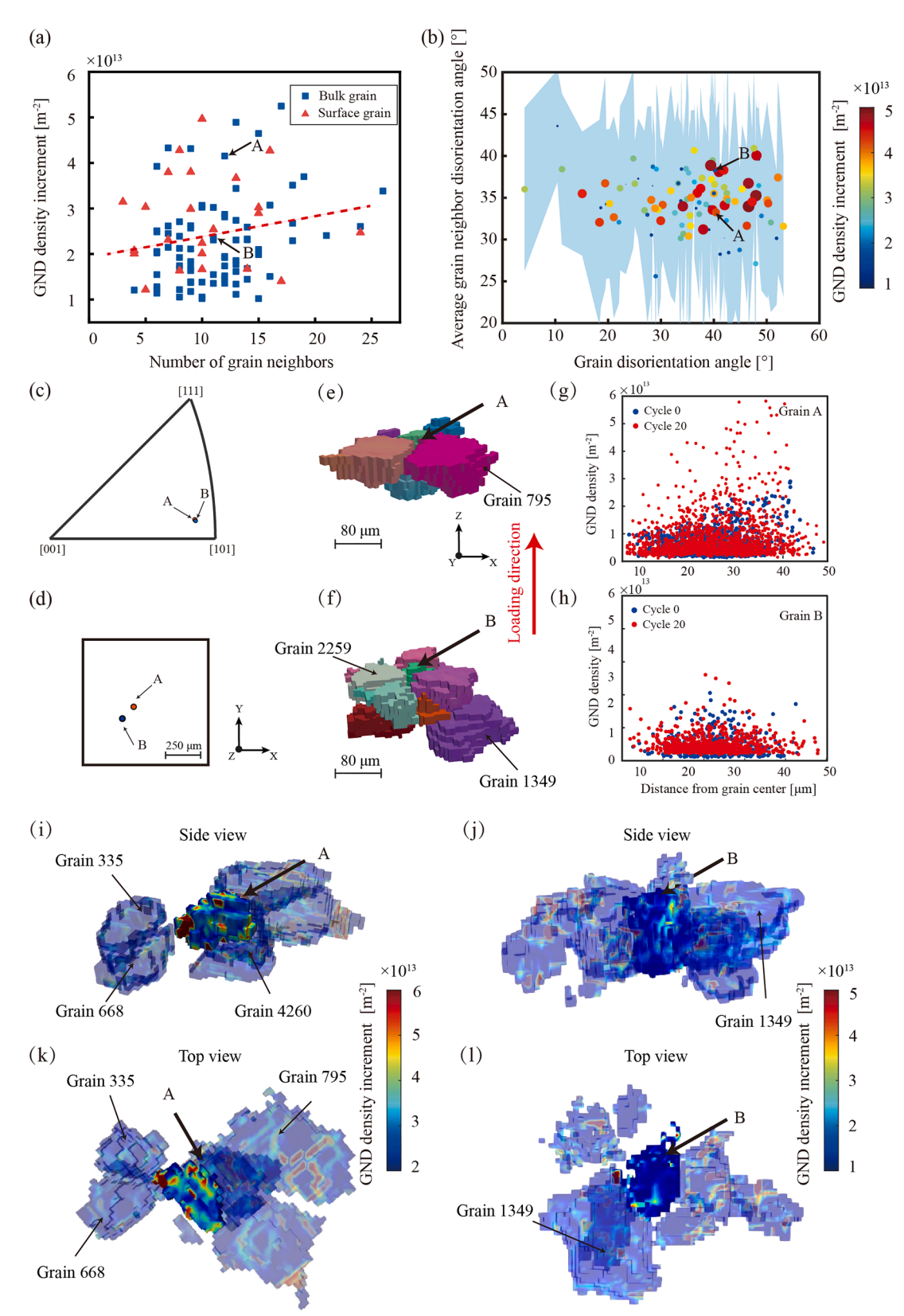


**Fig. 9.** Effect of grain neighborhood on GND density evolution. The number of grain neighbors versus increase in GND density between cycles 0 and 20 (a). The relationship between the grain disorientation angle (*x*-axis), grain neighbor disorientation angle (*y*-axis), and increase in GND density between cycles 0 and 20 (marker size and color) (b). The marker corresponds to the average grain neighbor disorientation, and the blue shaded areas show the standard deviation of the grain neighbor disorientation values. Two interiorly located grains with near identical orientation (c), position (d), and size yet showcase different GND density evolution behaviors (e,f). The GND density at each voxel for cycles 0 (blue) and 20 (red) versus the distance from the grain center for Grain A (g) and B (h). Side and top views illustrating the GND density increment of Grain A (i, k) and Grain B (k, l), along with their respective grain neighbors. (For interpretation of the references to color in this figure legend, the reader is referred to the web version of this article.)

f)), positions (Fig. 9(d)), and numbers of neighboring grains (Grain A has 12 neighbors and Grain B has 11 neighbors). Despite these similarities, these two grains have different neighborhoods and thus show different GND density evolution behavior. Fig. 9(g-h) shows the GND density at each voxel for cycles 0 and 20 versus the distance between the voxel and the grain centroid. Grain A has more GND density at cycle 20 than Grain B, and much of this GND density is close to the grain boundary (i.e., far from the grain centroid). Fig. 9(i-l) shows the spatially-resolved GND density for Grains A and B, as well as their respective grain neighbors. For Grain A, significant GND density is observed at the boundary between the "soft" Grain A and Grain 4260 (a "hard" grain, 18° grain disorientation). Grain A also has GND density accumulation near a triple junction shared with grains Grain 335 (a "soft" grain, 40° grain disorientation) and Grain 668 (a "soft" grain, 45° grain disorientation). For Grain B, there is very little GND density accumulation observed, and this GND density is distributed more uniformly across the grain (i.e., not localized near grain boundaries) compared with Grain A.

Based on these results, we hypothesize that the inability to transfer slip/transformation bands across a grain boundary between a soft-hard grain boundary may result in an increase in GND density in the soft grain, particularly near the grain boundary. In other words, the relatively high accumulation of GND density in Grain A is a result of strain

incompatibility between the soft grain and its hard neighborhood, and the relatively low accumulation of GND density in Grain B is a result of higher strain compatibility between the soft grain and its soft neighborhood. (This scenario is consistent with, e.g., the known phenomenon of slip-induced plastic dislocation pile-up observed (and considered detrimental) in hard-soft grain pairs, commonly termed as "rogue" grain pairs, found in nickel-based alloys and Ti-7Al, e.g., [75–77]). However, we acknowledge the limitations of comparing only two grains; the next section delves further into the influence of local grain boundary segments on the evolution of GND density.

#### 3.5. Effect of grain boundaries on GND density evolution

It is well known that grain boundaries are potential barriers for dislocation motion during plastic deformation, and the previous discussion suggests that this may be particularly true at a soft-hard grain boundary. Furthermore, the average GND density (as shown in, e.g., Figs. 6 and 9(g,h)) may not adequately reflect localized regions of high GND density accumulation at individual grain boundaries. In Fig. 10(a, b), we show the correlation between GND density in cycles 0 (blue) and 20 (red) versus distance from the closest grain boundary for all grains < 60  $\mu$ m (Fig. 10(a)) and > 60  $\mu$ m (Fig. 10(b)). The average GND density

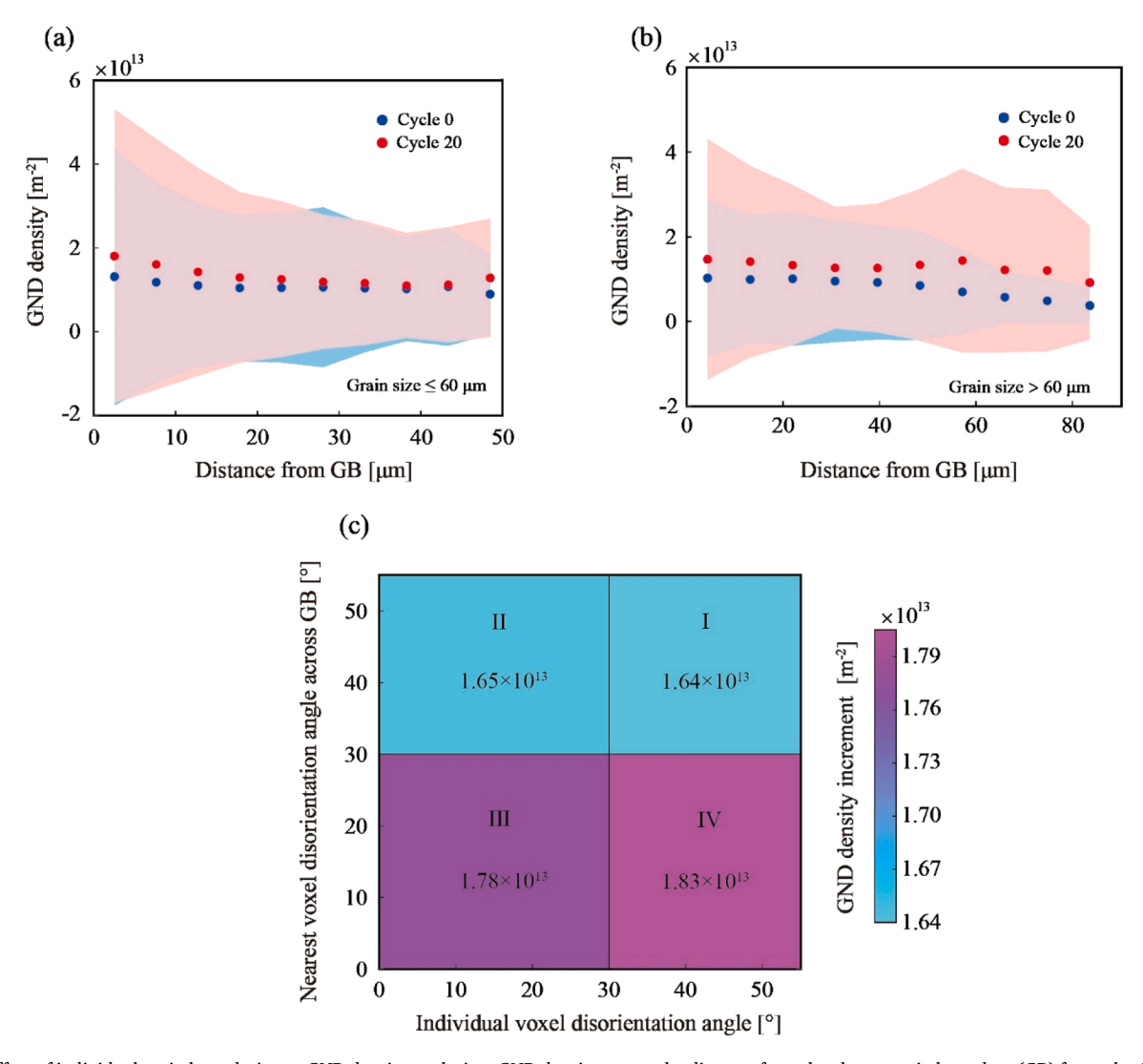


Fig. 10. Effect of individual grain boundaries on GND density evolution. GND density versus the distance from the closest grain boundary (GB) for cycles 0 and 20 for grains  $< 60 \ \mu m$  (a) and  $> 60 \ \mu m$  (b). Each marker shows the average, and the shaded regions show the standard deviation. Relationship between the disorientation angle of individual voxels within 15  $\mu m$  from the GB, the disorientation angle of the nearest voxel across the GB, and the average increase in GND density between cycles 0 and 20 (c).

(and the standard deviation) increases near boundaries for both grain size categories and for both cycles. Smaller (< 60 µm) grains exhibit a more pronounced increase near grain boundaries compared to larger (> 60 μm) grains. In Fig. 10(c), we analyzed the disorientation values and GND density accumulation only in voxels located within three voxels (15  $\mu$ m) from a grain boundary. We separate these  $\sim$ 57,000 voxels into four regions based on the disorientation angle of each voxel and that of its adjacent voxel across the GB: soft-soft disorientation pairs (Region I), hard-soft disorientation pairs (Region II), hard-hard disorientation pairs (Region III), and soft-hard disorientation pairs (Region IV), containing 24,602, 15,140, 6675, and 10,825 voxel pairs in each region, respectively. The results indicate that the disorientation difference across a grain boundary influences GND density accumulation. In particular, soft-soft disorientation pairs show the least accumulation of GND density, an observation that can possibly be explained by the easier transfer of dislocations during slip or martensitic transformation. Meanwhile, soft-hard disorientation pairs exhibit the highest accumulation, which reinforces our hypothesis about the strain compatibility effects induced by the grain boundary and its neighboring grains, as outlined in the previous section. The relatively low GND density accumulation observed in hard-soft and hard-hard disorientation pairs may be attributed to the reduced tendency of harder grains to emit dislocations. The results highlight the role of grain boundaries and the orientation differences across them on the evolution of GND density.

#### 4. Conclusions

A modified nf-HEDM algorithm was used to reconstruct 3D, spatially-resolved intragranular misorientation maps in a bulk Ni $_{49.9}$ Ti $_{50.1}$  polycrystalline shape memory alloy during twenty load-biased thermal cycles. These 3D maps of intragranular misorientation were then converted into 3D maps of GND density by calculating the dislocation density tensor components based on the measurements of orientation gradient. From these 3D maps, 120 grains with equivalent grain diameters from 40–160  $\mu$ m were selected for an investigation of the relationships between microstructure features and GND density accumulation during cycling. The major findings are summarized below:

- The intragranular misorientation reconstruction procedure was validated by performing a series of tests on synthetic diffraction data from a virtual "phantom" grain dataset. The results showed that spatially-resolved intragranular misorientation can be accurately reconstructed from nf-HEDM datasets even in the presence of significant plastic deformation (representing an improvement over conventional nf-HEDM analysis in this regard).
- The 120 grains exhibited heterogeneous GND density accumulation behavior, with some grains having relatively large GND density accumulation and others having relatively small GND density accumulation. The intragranular distribution of this GND density was also different for each grain, although in most grains, the GND density can be seen accumulating faster near grain boundaries.
- We found no strong correlation between the initial grain orientation and either the accumulation of GND density or the grain rotation. We also saw no strong correlation between GND density accumulation with either Schmid factor for plastic slip, or maximum

transformation work for martensitic transformation. These findings suggest that these widely accepted criteria for predicting mechanical behavior in SMAs may need to be re-evaluated.

- Grains that are close to the free surface and relatively large grains accumulate more GND density than interior (bulk) grains and relatively small grains, respectively.
- ullet By examining the average disorientation angle between a grain's neighboring grains  $<100>_{B2}$  axis and the loading direction, the findings reveal a weak correlation between GND density accumulation and the difference in disorientation angle between the central grain and its neighbors. An illustrative grain pair was chosen to explore the influence of individual grain neighbors, indicating that the intricacy of GND density accumulation at the interface and localized plastic deformation might diminish when local GND density is averaged across a grain.
- The influence of grain boundaries on GND density evolution was investigated by analyzing voxels near to grain boundaries. The results show an increase in average GND density (along with its standard deviation) near grain boundaries (versus far from grain boundaries) across all grain sizes and throughout the cycles. Notably, smaller grains (< 60 µm) demonstrate a more significant increase in GND density near grain boundaries compared to larger grains (> 60 µm). Also, voxels near grain boundaries exhibited the most GND density accumulation when they were located near soft-hard grain boundaries and the least GND density accumulation when they were located near soft-soft grain boundaries.

This work demonstrates the utility of nf-HEDM for understanding the evolution of intragranular structural changes in polycrystalline materials during thermomechanical loading, including those associated with geometrically necessary dislocations and martensitic phase transformation.

#### **Funding**

This material is based upon work supported by the National Science Foundation under award CMMI-2142302. This work is based upon research conducted at the Cornell High Energy Synchrotron Source which is supported by the National Science Foundation under award DMR-1332208.

#### Data availability

Data could be made available on request. The raw data cannot be shared at this time as the data also forms part of the ongoing study.

#### Declaration of competing interest

The authors declare no known competing interest.

#### Acknowledgements

The authors are grateful for helpful discussions with Prof. Aaron Stebner from the Georgia Institute of Technology, Department of Mechanical Engineering and Materials Science and Engineering.

#### Supplementary materials

Supplementary material associated with this article can be found, in the online version, at doi:10.1016/j.actamat.2024.119659.

#### Appendix A. Intragranular misorientation reconstruction validation

To validate the accuracy of intragranular misorientation reconstruction, a series of validation tests are performed using synthetic HEDM data. A virtual polycrystalline copper sample is deformed under tensile uniaxial loading to a strain of 10 %. The virtual copper sample is  $128 \times 128 \times 128$ 

voxels<sup>3</sup> with a voxel size of  $5 \times 5 \times 5 \,\mu\text{m}^3$ . From this polycrystal, a grain with an orientation spread larger than  $5^\circ$  in the deformed state is selected, and this grain and its surrounding neighborhood (a total volume of interest of  $41 \times 41$  voxels) are used to synthesize virtual HEDM data sets. A schematic of nf-HEDM experimental setup for virtual diffraction is shown in Fig. A1. The sample-to-detector distances and detector/pixel sizes are kept the same as our experimental parameters. The incident beam travels along the negative  $e_z$  direction (see Fig. A1), and the virtual sample is positioned at the origin of the laboratory coordinate system, without any tilt angles, and is rotated about the  $e_y$  axis. The HEDM diffraction images are generated using the virtual diffraction method [46,49] by rotating the sample every  $0.25^\circ$  for a total rotation of  $360^\circ$ . Two different beam sizes, a 1D "line" beam ( $\sim 5 \times 205 \,\mu\text{m}^2$ ) and a 2D "box" beam ( $\sim 175 \times 205 \,\mu\text{m}^2$ ), both with an energy of 55.618 keV, are simulated to illuminate the layer of interest (in the line beam scenarios) and volume of interest (in the box beam scenarios) in the virtual sample both before and after deformation.

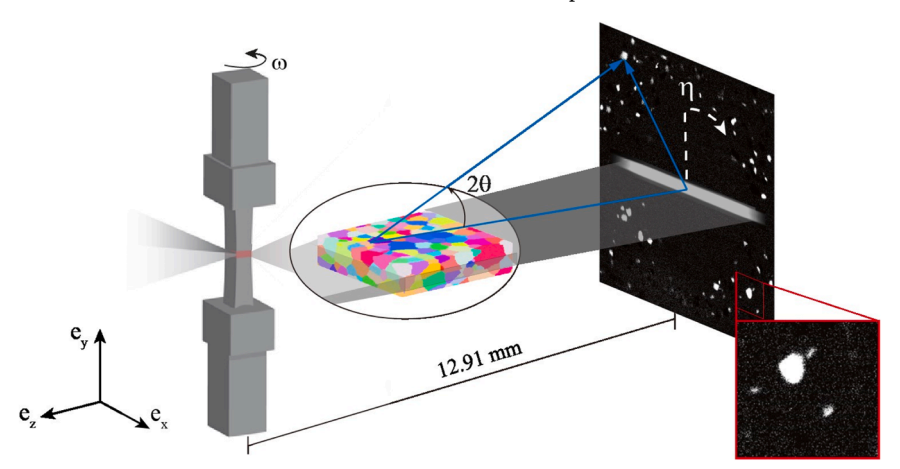


Fig. A1. Schematic of nf-HEDM experimental setup for virtual diffraction. The laboratory reference coordinate system is shown with x, y, z subscripts. The diffraction angle  $2\theta$ , sample rotation angle  $\omega$ , and azimuthal angle  $\eta$  are shown. The origin of the laboratory coordinate system is aligned with the center of the intersection between the incident beam and the virtual sample. To synthesize the HEDM diffraction images, the sample is rotated about  $e_y$  while HEDM diffraction images are integrated over every  $0.25^{\circ}$  over a total rotation of  $360^{\circ}$ .

The central layer in the four scenarios (undeformed microstructure with a line beam, undeformed microstructure with a box beam, deformed microstructure with a line beam, and deformed microstructure with a box beam) are reconstructed using the specialized intragranular misorientation analysis procedure described in the main manuscript and compared with the original synthetic microstructure input. The results are shown in Fig. A2, Fig. A3, and Fig. A4 for the box beam scenarios and Fig. S2 and S3 for the line beam scenarios. To reconstruct the region of interest, a virtual grid with a dimension of  $81 \times 81$  voxels (including dilated region) with a voxel size of  $5 \times 5 \, \mu m^2$  is generated. The original orientation list from the undeformed microstructure is utilized as grain-averaged orientation candidates for peak indexing at each voxel as described in Section 2.2 in the manuscript. Then, a list of trial orientations with an angular spread of  $\pm 5^{\circ}$  and a spacing of  $0.25^{\circ}$  along each direction in Rodrigues space is generated and tested at each voxel (also as described in Section 2.2). The orientation with the highest completeness (> 0.8) is assigned to each voxel.

The results for the undeformed microstructure with the 2D box beam and 1D line beam are shown in Fig. A2 and Fig. S2, respectively. The input synthetic microstructure exhibits uniform orientation distribution across each grain as shown in Fig. A2(a,b). The nf-HEDM images in Fig. A2(d) and Fig. S2(d) show what the virtual Bragg reflections belonging to the layer of interest look like. Using the intragranular misorientation reconstruction method described in the manuscript, the spatially-resolved orientation is reconstructed in Fig. A2(c) and Fig. S2(c). The uniform orientation distribution is successfully captured by the intragranular misorientation algorithm. To compare the input versus reconstructed grain boundary positions, the input and the reconstructed grain boundaries are plotted together in Fig. A2(e,f) and Fig. S2(e,f). Comparing the reconstructed grain boundaries to the real grain boundaries across the cross-section, the discrepancies are, on average, less than 1 voxel (5  $\mu$ m) apart from each other. Thus, the results show that both the grain shape and the spatially-resolved orientation distribution is well reconstructed in both of the undeformed microstructure scenarios.

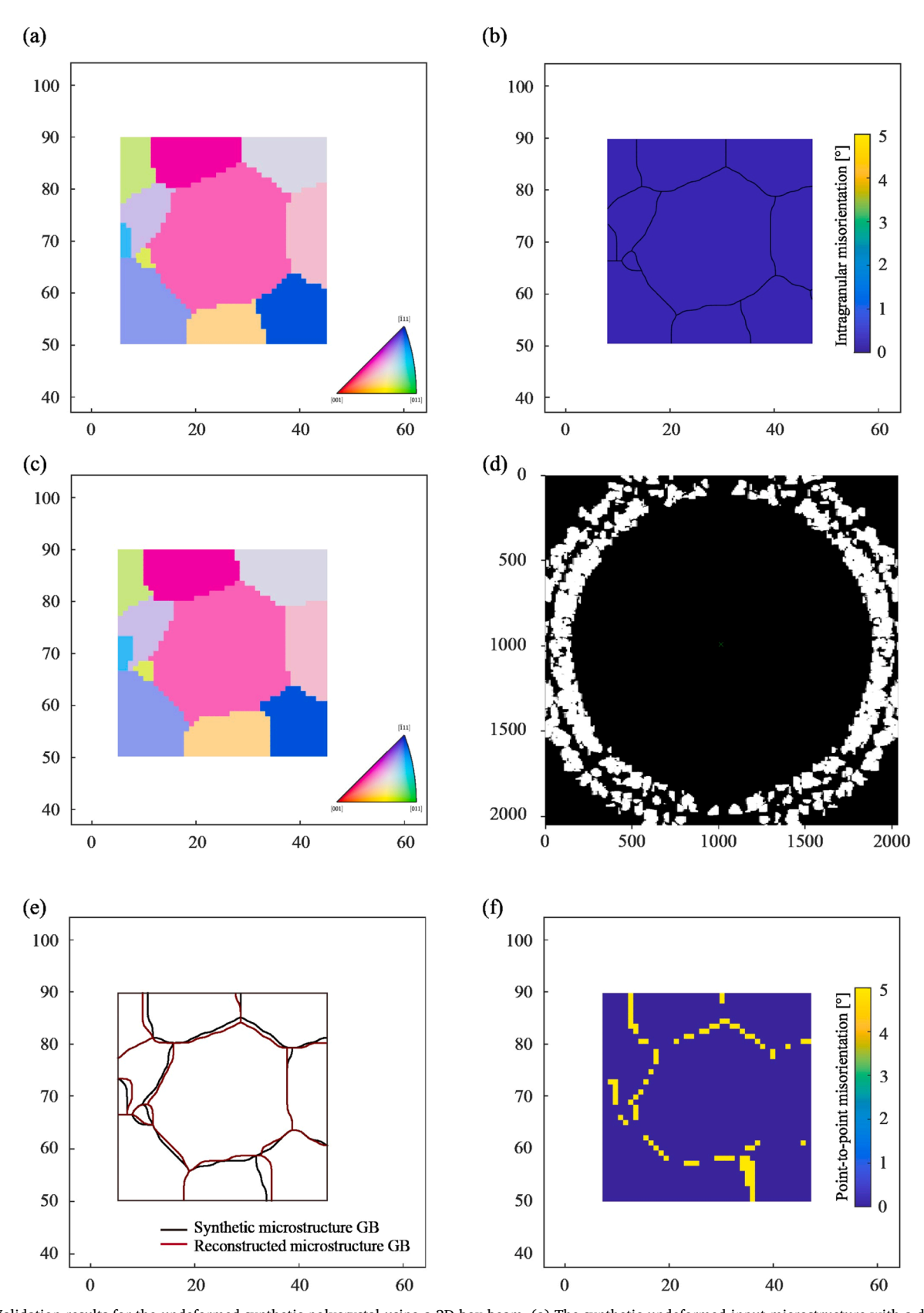


Fig. A2. Validation results for the undeformed synthetic polycrystal using a 2D box beam. (a) The synthetic undeformed input microstructure with a dimension of  $41\times41$  voxels with a voxel size of  $5\times5$   $\mu\text{m}^2$ . (b) Intragranular misorientation map of the input microstructure. (c) Reconstructed spatially-resolved orientation map of the undeformed microstructure using the intragranular misorientation analysis procedure presented in this work. (d) The virtual nf-HEDM images (summed over a complete rotation of  $360^\circ$ ). (e) Grain boundary position comparison between the input synthetic (black) and reconstructed (red) microstructures. (f) Point-to-point misorientation comparison between the input and reconstructed orientation maps.

The results for the deformed (10 % strain) microstructure with the 2D box beam and 1D line beam are shown in Fig. A3 and Fig. S3, respectively.

The plastically deformed microstructure has an orientation spread of over  $5^{\circ}$  in each grain as shown in Fig. A3(a,b). The nf-HEDM images in Fig. A3(d) and Fig. S3(d) show that the deformed Bragg reflections are now smeared in the azimuthal direction due to the orientation spread. (Not shown: The Bragg reflections are also spread between images, i.e., in the  $\omega$  direction.) Using the intragranular misorientation analysis procedure described in the manuscript, the spatially-resolved orientation is reconstructed in Fig. A3(c) and Fig. S3(c). To compare the input versus reconstructed grain boundary positions, the input and the reconstructed grain boundaries are plotted together in Fig. A3(e,f) and Fig. S3(e,f). The comparison shows that the input versus reconstructed grain boundaries are on average less than 1 voxel (5  $\mu$ m) apart from each other. As anticipated, the central region of each grain exhibits a relatively low point-to-point misorientation magnitude. However, at the grain boundaries and missing point regions, the reconstruction accuracy decreases due to the presence of severe plastic deformation [37,78]. The reconstruction quality in deformed microstructure can be further promoted by refining the virtual grid size and Monte Carlo optimization [42]. However, integrating this and retesting ~1000 trial orientations at each finely meshed voxel would significantly extend the computation time. Balancing the reconstruction quality and the overall computation time, we believe that intragranular misorientation reconstruction is reasonable for this case [79,80].

To compare the reconstruction accuracy in each scenario, cumulative distribution of point-to-point misorientation results are plotted in Fig. A4(a). The findings suggest that the performance of the intragranular misorientation algorithm in the 1D line beam scenario is better than in the 2D box beam scenario. Although there is a shift in the cumulative distribution of misorientation angle toward larger values in the 2D box beam deformed microstructure reconstruction, nearly 90 % of the data points for the reconstructed undeformed and deformed microstructure are located within  $5^{\circ}$  misorientation (Fig. A4(b)). It is important to emphasize that in the deformed microstructure scenarios, the level of deformation has exceeded the limits of the current conventional nf-HEDM analysis, which typically handles strains up to 2-3 % [81]. However, the specialized intragranular misorientation reconstruction procedure still yields reliable results, despite 10 % strains, and thus marks a significant improvement when plastic deformation is of interest. Finally, in cases where studying significant plastic deformation with increased spatial resolution (<1  $\mu$ m) is needed, alternative methods such as scanning 3DXRD [82–85] or point-focused HEDM (pf-HEDM) [70] can be explored.

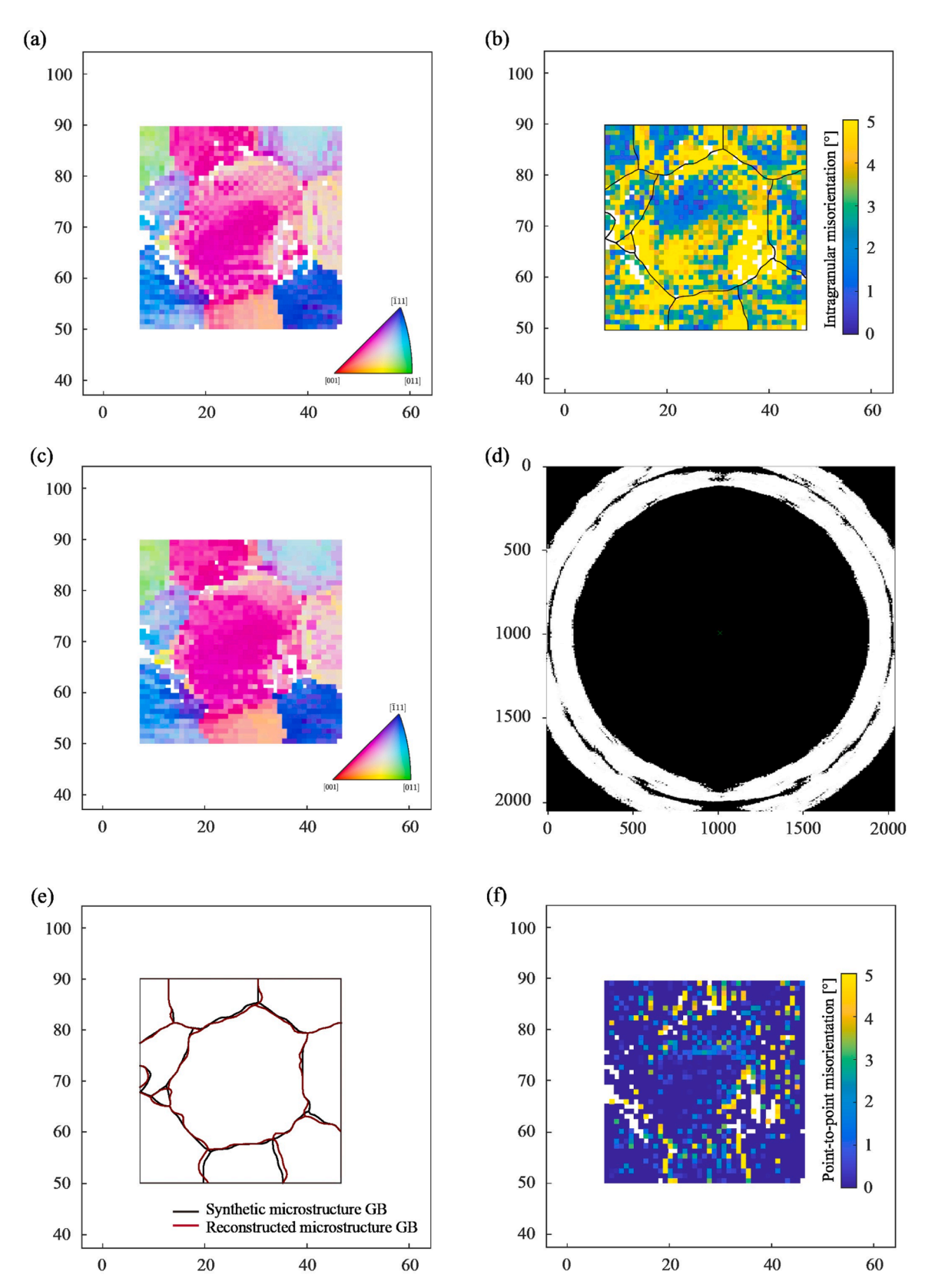


Fig. A3. Validation results for the deformed synthetic polycrystal using a 2D box beam. (a) The synthetic deformed microstructure with a dimension of  $41 \times 41$  voxels with a voxel size of  $5 \times 5 \mu m^2$ . (b) Intragranular misorientation map of the input microstructure. (c) Reconstructed spatially-resolved orientation map of the deformed microstructure using the intragranular misorientation analysis procedure presented in this work. (d) The virtual nf-HEDM images (summed over a complete rotation of  $360^{\circ}$ ). (e) Grain boundary position comparison between the input synthetic (black) and reconstructed (red) microstructures. (f) Point-to-point misorientation comparison between the input and reconstructed orientation maps. The white data points represent either missing data points in (a-b) or reconstructed data points with a confidence level below the threshold of 0.8 in (c).

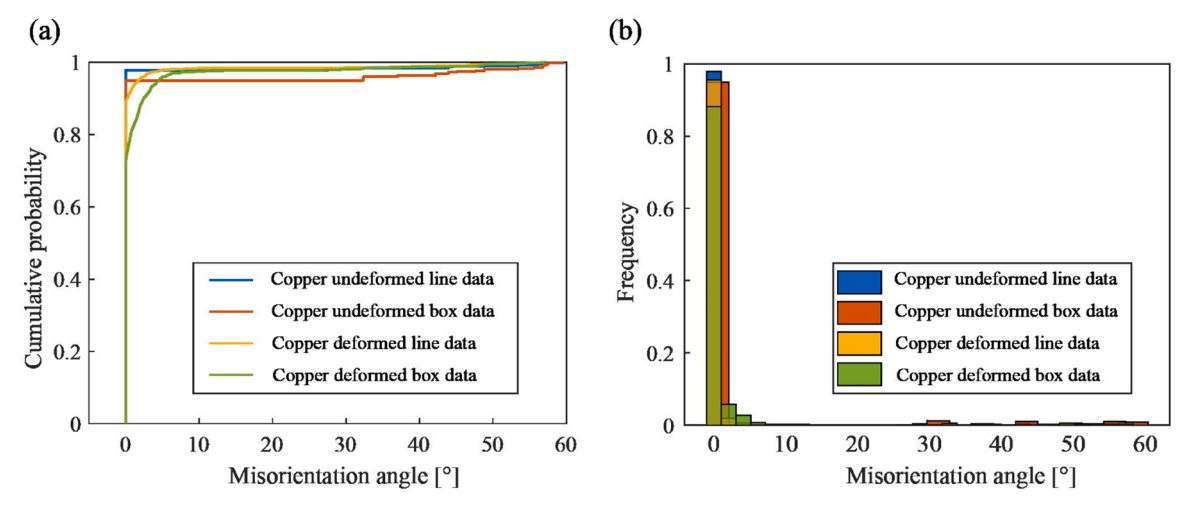


Fig. A4. Statistical analysis of point-to-point misorientation between the input and the microstructures reconstructed using the intragranular misorientation procedure presented in the manuscript. (a) Cumulative misorientation distribution across the region of interest in each of the four scenarios. (b) Histogram of point-to-point misorientation.

Finally, we note that this virtual validation study does not include various experimental complications such as detector noise and incident beam imperfections, and dedicated, in-depth experimental validation studies are greatly needed in the HEDM and larger diffraction microstructure imaging communities. Focused experimental HEDM validation studies using complementary techniques like serial section electron backscatter diffraction are currently being pursued the authors, as well as the International Union of Crystallography (IUCr) commission on Diffraction Microstructure Imaging (DMI), and will be published in the near future.

#### References

- [1] K. Otsuka, X. Ren, Recent developments in the research of shape memory alloys, Intermetallics 7 (1999) 511–528, https://doi.org/10.1016/S0966-9795(98)00070-3
- [2] K. Otsuka, C.M. Wayman, Shape Memory Materials, Cambridge University Press, 1999.
- [3] T.W. Duerig, K.N. Melton, D. Stöckel, Engineering Aspects of Shape Memory Alloys, Butterworth-Heinemann, 2013.
- [4] C.S. Haines, M.D. Lima, N. Li, G.M. Spinks, J. Foroughi, J.D.W. Madden, S.H. Kim, S. Fang, M. Jung de Andrade, F. Göktepe, Ö. Göktepe, S.M. Mirvakili, S. Naficy, X. Lepró, J. Oh, M.E. Kozlov, S.J. Kim, X. Xu, B.J. Swedlove, G.G. Wallace, R. H. Baughman, Artificial muscles from fishing line and sewing thread, Science 343 (2014) 868–872, https://doi.org/10.1126/science.1246906.
- [5] Y. Kim, G.A. Parada, S. Liu, X. Zhao, Ferromagnetic soft continuum robots, Sci. Robot. 4 (2019) eaax7329, https://doi.org/10.1126/scirobotics.aax7329.
- [6] D. Grant, V. Hayward, Variable structure control of shape memory alloy actuators, IEEE Control Syst. Mag. 17 (1997) 80–88, https://doi.org/10.1109/37.588180.
- [7] D. Stoeckel, A. Pelton, T. Duerig, Self-expanding nitinol stents: material and design considerations, Eur. Radiol. 14 (2004) 292–301, https://doi.org/10.1007/s00330-003-2022-5
- [8] M. Sreekumar, T. Nagarajan, M. Singaperumal, M. Zoppi, R. Molfino, Critical review of current trends in shape memory alloy actuators for intelligent robots, Ind. Robot Int. J. 34 (2007) 285–294, https://doi.org/10.1108/01439910710749609.
- [9] D. Hartl J, D.C. Lagoudas, Aerospace applications of shape memory alloys, Proc. Inst. Mech. Eng. Part G J. Aerosp. Eng. 221 (2007) 535–552, https://doi.org/ 10.1243/09544100JAERO211.
- [10] T. Duerig, A. Pelton, D. Stöckel, An overview of nitinol medical applications, Mater. Sci. Eng. A 273–275 (1999) 149–160, https://doi.org/10.1016/S0921-5093 (2010)204.4
- [11] T. Yoneyama, S. Miyazaki, Shape Memory Alloys for Biomedical Applications, Elsevier, 2008.
- [12] S. Shabalovskaya, J. Anderegg, J. Van Humbeeck, Critical overview of Nitinol surfaces and their modifications for medical applications, Acta Biomater. 4 (2008) 447–467. https://doi.org/10.1016/j.actbio.2008.01.013.
- [13] K. Otsuka, X. Ren, Physical metallurgy of Ti-Ni-based shape memory alloys, Prog. Mater. Sci. 50 (2005) 511–678, https://doi.org/10.1016/j.pmatsci.2004.10.001.
- [14] G. Eggeler, E. Hornbogen, A. Yawny, A. Heckmann, M. Wagner, Structural and functional fatigue of NiTi shape memory alloys, Mater. Sci. Eng. A 378 (2004) 24–33, https://doi.org/10.1016/j.msea.2003.10.327.
- [15] S.W. Robertson, A.R. Pelton, R.O. Ritchie, Mechanical fatigue and fracture of Nitinol, Int. Mater. Rev. 57 (2012) 1–36, https://doi.org/10.1179/ 1743280411Y.0000000009.
- [16] Y. Gao, L. Casalena, M.L. Bowers, R.D. Noebe, M.J. Mills, Y. Wang, An origin of functional fatigue of shape memory alloys, Acta Mater. 126 (2017) 389–400, https://doi.org/10.1016/j.actamat.2017.01.001.

- [17] J. Frenzel, On the importance of structural and functional fatigue in shape memory technology, Shape Mem. Superelast. 6 (2020) 213–222, https://doi.org/10.1007/ s40830-020-00281-3.
- [18] A.R. Pelton, Nitinol fatigue: a review of microstructures and mechanisms, J. Mater. Eng. Perform. 20 (2011) 613–617, https://doi.org/10.1007/s11665-011-9864-9.
- [19] P. Hua, M. Xia, Y. Onuki, Q. Sun, Nanocomposite NiTi shape memory alloy with high strength and fatigue resistance, Nat. Nanotechnol. 16 (2021) 409–413, https://doi.org/10.1038/s41565-020-00837-5.
- [20] C.N. Saikrishna, K.V. Ramaiah, B. Vidyashankar, S.K. Bhaumik, N.A. Laboratories, M.S. Division, G. Motors, Functional fatigue in NiTi shape memory alloy wires a comparative study, in: Natl. Conf. Smart Mater. Struct. Syst. Sept. 21-22 Coimbatore India Funct, 2012, pp. 1–6.
- [21] T. Yu, Y. Gao, L. Casalena, P. Anderson, M. Mills, Y. Wang, H-phase precipitation and its effects on martensitic transformation in NiTi-Hf high-temperature shape memory alloys, Acta Mater. 208 (2021) 116651, https://doi.org/10.1016/j. actamat.2021.116651.
- [22] J.F. Nye, Some geometrical relations in dislocated crystals, Acta Metall. 1 (1953) 153–162, https://doi.org/10.1016/0001-6160(53)90054-6.
- [23] M.F. Ashby, The deformation of plastically non-homogeneous materials, Philos. Mag. J. Theor. Exp. Appl. Phys. 21 (1970) 399–424, https://doi.org/10.1080/ 14786437008238426.
- [24] F.R. Phillips, R.W. Wheeler, A.B. Geltmacher, D.C. Lagoudas, Evolution of internal damage during actuation fatigue in shape memory alloys, Int. J. Fatigue 124 (2019) 315–327, https://doi.org/10.1016/j.ijfatigue.2018.12.019.
- [25] M.L. Bowers, Y. Gao, L. Yang, D.J. Gaydosh, M. De Graef, R.D. Noebe, Y. Wang, M. J. Mills, Austenite grain refinement during load-biased thermal cycling of a Ni49.9Ti50.1 shape memory alloy, Acta Mater. 91 (2015) 318–329, https://doi.org/10.1016/j.actamat.2015.03.017.
- [26] S. Berveiller, B. Malard, J. Wright, E. Patoor, G. Geandier, In situ synchrotron analysis of lattice rotations in individual grains during stress-induced martensitic transformations in a polycrystalline CuAlBe shape memory alloy, Acta Mater. 59 (2011) 3636–3645, https://doi.org/10.1016/j.actamat.2011.02.037.
- [27] Y. El Hachi, S. Berveiller, B. Piotrowski, J. Wright, W. Ludwig, B. Malard, Multi-scale in situ mechanical investigation of the superelastic behavior of a Cu-Al-Be polycrystalline shape memory alloy, Acta Mater. 235 (2022) 118107, https://doi.org/10.1016/j.actamat.2022.118107.
- [28] P. Sedmák, J. Pilch, L. Heller, J. Kopeček, J. Wright, P. Sedlák, M. Frost, P. Šittner, Grain-resolved analysis of localized deformation in nickel-titanium wire under tensile load, Science 353 (2016) 559–562, https://doi.org/10.1126/science. 2016/700
- [29] H.M. Paranjape, P.P. Paul, B. Amin-Ahmadi, H. Sharma, D. Dale, J.Y.P. Ko, Y. I. Chumlyakov, L.C. Brinson, A.P. Stebner, In situ, 3D characterization of the deformation mechanics of a superelastic NiTi shape memory alloy single crystal under multiscale constraint, Acta Mater 144 (2018) 748–757, https://doi.org/10.1016/j.actamat.2017.11.026.
- [30] H.M. Paranjape, P.P. Paul, H. Sharma, P. Kenesei, J.-S. Park, T.W. Duerig, L. C. Brinson, A.P. Stebner, Influences of granular constraints and surface effects on the heterogeneity of elastic, superelastic, and plastic responses of polycrystalline

- shape memory alloys, J. Mech. Phys. Solids 102 (2017) 46–66, https://doi.org/
- [31] A.N. Bucsek, D. Dale, J.Y.P. Ko, Y. Chumlyakov, A.P. Stebner, Measuring stressinduced martensite microstructures using far-field high-energy diffraction microscopy, Acta Crystallogr. Sect. Found. Adv. 74 (2018) 425–446, https://doi. org/10.1107/S205327331800880X.
- [32] A.N. Bucsek, D.C. Pagan, L. Casalena, Y. Chumlyakov, M.J. Mills, A.P. Stebner, Ferroelastic twin reorientation mechanisms in shape memory alloys elucidated with 3D X-ray microscopy, J. Mech. Phys. Solids 124 (2019) 897–928, https://doi. org/10.1016/j.jmps.2018.12.003.
- [33] A.N. Bucsek, L. Casalena, D.C. Pagan, P.P. Paul, Y. Chumlyakov, M.J. Mills, A. P. Stebner, Three-dimensional in situ characterization of phase transformation induced austenite grain refinement in nickel-titanium, Scr. Mater. 162 (2019) 361–366, https://doi.org/10.1016/j.scriptamat.2018.11.043.
- [34] W. He, W. Ma, W. Pantleon, Microstructure of individual grains in cold-rolled aluminium from orientation inhomogeneities resolved by electron backscattering diffraction, Mater. Sci. Eng. A 494 (2008) 21–27, https://doi.org/10.1016/j. mses. 2007.10.092
- [35] P.J. Konijnenberg, S. Zaefferer, D. Raabe, Assessment of geometrically necessary dislocation levels derived by 3D EBSD, Acta Mater. 99 (2015) 402–414, https:// doi.org/10.1016/j.actamat.2015.06.051.
- [36] M. Calcagnotto, D. Ponge, E. Demir, D. Raabe, Orientation gradients and geometrically necessary dislocations in ultrafine grained dual-phase steels studied by 2D and 3D EBSD, Mater. Sci. Eng. A 527 (2010) 2738–2746, https://doi.org/ 10.1016/j.msea.2010.01.004.
- [37] S.F. Li, J. Lind, C.M. Hefferan, R. Pokharel, U. Lienert, A.D. Rollett, R.M. Suter, Three-dimensional plastic response in polycrystalline copper via near-field highenergy X-ray diffraction microscopy, J. Appl. Crystallogr. 45 (2012) 1098–1108, https://doi.org/10.1107/S0021889812039519.
- [38] J Oddershede, B. Camin, S. Schmidt, L.P.. Mikkelsen, H.O. Sørensen, U. Lienert, Reimers, General rights measuring the stress field around an evolving crack in tensile deformed Mg AZ31 using three-dimensional X-ray diffraction measuring the stress field around an evolving crack in tensile deformed Mg AZ31 using 3DXRD, Citation (2012), https://doi.org/10.1016/j.actamat.2012.02.054.
- [39] D.P. Naragani, P.A. Shade, P. Kenesei, H. Sharma, M.D. Sangid, X-ray characterization of the micromechanical response ahead of a propagating small fatigue crack in a Ni-based superalloy, Acta Mater. 179 (2019) 342–359, https:// doi.org/10.1016/i.actamat.2019.08.005.
- [40] V. Prithivirajan, P. Ravi, D. Naragani, M.D. Sangid, Direct comparison of microstructure-sensitive fatigue crack initiation via crystal plasticity simulations and in situ high-energy X-ray experiments, Mater. Des. 197 (2021) 109216, https://doi.org/10.1016/j.matdes.2020.109216.
- [41] P. Ravi, D. Naragani, P. Kenesei, J.-S. Park, M.D. Sangid, Direct observations and characterization of crack closure during microstructurally small fatigue crack growth via in-situ high-energy X-ray characterization, Acta Mater. 205 (2021) 116564. https://doi.org/10.1016/j.actamat.2020.116564.
- [42] R.M. Suter, D. Hennessy, C. Xiao, U. Lienert, Forward modeling method for microstructure reconstruction using x-ray diffraction microscopy: single-crystal verification, Rev. Sci. Instrum. 77 (2006) 123905, https://doi.org/10.1063/ 1.2400017
- [43] HEXOMAP HeLiuCMU, High Energy X-ray Orientation Mapping, 2023. https://github.com/HeLiuCMU/HEXOMAP (Accessed 5 January 2024).
- [44] P. Avery, B. Major, S. Singh, C. Harris, M.D. Hanwell, J. Tourtellott, K. Nygren, P. Shade, J. Bernier, HEXRD/hexrdgui: Release 0.9.6, 2023, https://doi.org/ 10.5281/ZENODO 8034775
- [45] J. Bernier, P. Avery, S. Singh, C. Harris, R. Lim, D. Pagan, D. Boyce, B. Major, J. Tourtellot, Ó.V. Guillén, R. Rygg, K. Nygren, P. Shade, HEXRD/hexrd: Release 0.9.3, 2023, https://doi.org/10.5281/ZENODO.8033940.
- [46] K.E. Nygren, D.C. Pagan, J.V. Bernier, M.P. Miller, An algorithm for resolving intragranular orientation fields using coupled far-field and near-field high energy X-ray diffraction microscopy, Mater. Charact. 165 (2020) 110366, https://doi.org/ 10.1016/j.matchar.2020.110366.
- [47] P.A. Shade, B. Blank, J.C. Schuren, T.J. Turner, P. Kenesei, K. Goetze, R.M. Suter, J. V. Bernier, S.F. Li, J. Lind, U. Lienert, J. Almer, A rotational and axial motion system load frame insert for in situ high energy x-ray studies, Rev. Sci. Instrum. 86 (2015) 093902, https://doi.org/10.1063/1.4927855.
- [48] U. Ayachit, The paraview guide: a parallel visualization application, Kitware, Inc. 2015 https://doi.org/10.5555/2789330
- [49] S.L. Wong, J.-S. Park, M.P. Miller, P.R. Dawson, A framework for generating synthetic diffraction images from deforming polycrystals using crystal-based finite element formulations, Comput. Mater. Sci. 77 (2013) 456–466, https://doi.org/ 10.1016/j.commatsci.2013.03.019.
- [50] J.V. Bernier, N.R. Barton, U. Lienert, M.P. Miller, Far-field high-energy diffraction microscopy: a tool for intergranular orientation and strain analysis, J. Strain Anal. Eng. Des. 46 (2011) 527–547, https://doi.org/10.1177/0309324711405761.
- [51] W. Pantleon, Resolving the geometrically necessary dislocation content by conventional electron backscattering diffraction, Scr. Mater. 58 (2008) 994–997, https://doi.org/10.1016/j.scriptamat.2008.01.050.
- [52] A.J. Wilkinson, D. Randman, Determination of elastic strain fields and geometrically necessary dislocation distributions near nanoindents using electron back scatter diffraction, Philos. Mag. 90 (2010) 1159–1177, https://doi.org/ 10.1080/14786430903304145.
- [53] T. Benjamin Britton, A.J. Wilkinson, Stress fields and geometrically necessary dislocation density distributions near the head of a blocked slip band, Acta Mater. 60 (2012) 5773–5782, https://doi.org/10.1016/j.actamat.2012.07.004.

- [54] J. Jiang, T.B. Britton, A.J. Wilkinson, The orientation and strain dependence of dislocation structure evolution in monotonically deformed polycrystalline copper, Int. J. Plast. 69 (2015) 102–117, https://doi.org/10.1016/j.ijplas.2015.02.005.
- [55] Y. Guo, D.M. Collins, E. Tarleton, F. Hofmann, A.J. Wilkinson, T.B. Britton, Dislocation density distribution at slip band-grain boundary intersections, Acta Mater. 182 (2020) 172–183, https://doi.org/10.1016/j.actamat.2019.10.031.
- [56] F. Bachmann, R. Hielscher, H. Schaeben, Texture analysis with MTEX free and open source software toolbox, Solid State Phenom. 160 (2010) 63–68, https://doi. org/10.4028/www.scientific.net/SSP.160.63.
- [57] R. Hielscher, C.B. Silbermann, E. Schmidl, J. Ihlemann, Denoising of crystal orientation maps, J. Appl. Crystallogr. 52 (2019) 984–996, https://doi.org/ 10.1107/51600576710000075
- [58] H. Sehitoglu, Y. Wu, S. Alkan, E. Ertekin, Plastic deformation of B2-NiTi-is it slip or twinning? Philos. Mag. Lett. 97 (2017) 217–228, https://doi.org/10.1080/ 09500839 2017 1316019
- [59] T. Ezaz, J. Wang, H. Sehitoglu, H.J. Maier, Plastic deformation of NiTi shape memory alloys, Acta Mater. 61 (2013) 67–78, https://doi.org/10.1016/j. actamat.2012.09.023.
- [60] O. Benafan, R.D. Noebe, S.A. Padula, A. Garg, B. Clausen, S. Vogel, R. Vaidyanathan, Temperature dependent deformation of the B2 austenite phase of a NiTi shape memory alloy, Int. J. Plast. 51 (2013) 103–121, https://doi.org/ 10.1016/j.ijplas.2013.06.003.
- [61] A. Bucsek, H. Seiner, H. Simons, C. Yildirim, P. Cook, Y. Chumlyakov, C. Detlefs, A. P. Stebner, Sub-surface measurements of the austenite microstructure in response to martensitic phase transformation, Acta Mater. 179 (2019) 273–286, https://doi.org/10.1016/j.actamat.2019.08.036.
- [62] X. Chen, V. Srivastava, V. Dabade, R.D. James, Study of the cofactor conditions: conditions of supercompatibility between phases, J. Mech. Phys. Solids 61 (2013) 2566–2587, https://doi.org/10.1016/j.jmps.2013.08.004.
- [63] K. Oishi, L.C. Brown, Stress-induced martensite formation in Cu–Al–Ni alloys, Metall. Trans. 2 (1971) 1971–1977, https://doi.org/10.1007/BF02913432.
- [64] K. Okamoto, S. Ichinose, K. Morii, K. Otsuka, K. Shimizu, Crystallography of β1 → γ'1 stress-induced martensitic transformation in a Cu-Al-Ni alloy, Acta Metall. 34 (1986) 2065–2073, https://doi.org/10.1016/0001-6160(86)90265-8.
- [65] T.W. Shield, Orientation dependence of the pseudoelastic behavior of single crystals of Cu-Al-Ni in tension, J. Mech. Phys. Solids 43 (1995) 869–895, https:// doi.org/10.1016/0022-5096(95)00011-7.
- [66] X.Y. Zhang, L.C. Brinson, Q.P. Sun, The variant selection criteria in single-crystal CuAlNi shape memory alloys, Smart Mater. Struct. 9 (2000) 571–581, https://doi. org/10.1088/0964-1726/9/5/301.
- [67] J. Lind, S.F. Li, R. Pokharel, U. Lienert, A.D. Rollett, R.M. Suter, Tensile twin nucleation events coupled to neighboring slip observed in three dimensions, Acta Mater. 76 (2014) 213–220, https://doi.org/10.1016/J.ACTAMAT.2014.04.050.
- [68] I.J. Beyerlein, L. Capolungo, P.E. Marshall, R.J. McCabe, C.N. Tomé, Statistical analyses of deformation twinning in magnesium, Philos. Mag. 90 (2010) 2161–2190, https://doi.org/10.1080/14786431003630835.
- [69] L. Nervo, A. King, A. Fitzner, W. Ludwig, M. Preuss, A study of deformation twinning in a titanium alloy by X-ray diffraction contrast tomography, Acta Mater. 105 (2016) 417–428. https://doi.org/10.1016/j.actamat.2015.12.032
- 105 (2016) 417-428, https://doi.org/10.1016/j.actamat.2015.12.032.
   [70] W. Li, H. Sharma, K. Peter, S. Ravi, H. Sehitoglu, A. Bucsek, Resolving intragranular stress fields in plastically deformed titanium using point-focused high-energy diffraction microscopy, J. Mater. Res. 38 (2023) 165-178, https://doi.org/10.1557/43578-022-00873-v
- [71] J.C. Stinville, W. Ludwig, P.G. Callahan, M.P. Echlin, V. Valle, T.M. Pollock, H. Proudhon, Observation of bulk plasticity in a polycrystalline titanium alloy by diffraction contrast tomography and topotomography, Mater. Charact. 188 (2022) 111891, https://doi.org/10.1016/j.matchar.2022.111891.
  [72] L. Wang, Z. Zheng, H. Phukan, P. Kenesei, J.-S. Park, J. Lind, R.M. Suter, T.
- [72] L. Wang, Z. Zheng, H. Phukan, P. Kenesei, J.-S. Park, J. Lind, R.M. Suter, T. R. Bieler, Direct measurement of critical resolved shear stress of prismatic and basal slip in polycrystalline Ti using high energy X-ray diffraction microscopy, Acta Mater. 132 (2017) 598–610, https://doi.org/10.1016/j.actamat.2017.05.015.
- [73] H. Paranjape, P.M. Anderson, Texture and grain neighborhood effects on Ni–Ti shape memory alloy performance, Model. Simul. Mater. Sci. Eng. 22 (2014) 075002, https://doi.org/10.1088/0965-0393/22/7/075002.
- [74] A.N. Bucsek, H.M. Paranjape, A.P. Stebner, Myths and truths of nitinol mechanics: elasticity and tension-compression asymmetry, Shape Mem. Superelast. 2 (2016) 264–271, https://doi.org/10.1007/s40830-016-0074-z.
- [75] S. Birosca, F. Di Gioacchino, S. Stekovic, M. Hardy, A quantitative approach to study the effect of local texture and heterogeneous plastic strain on the deformation micromechanism in RR1000 nickel-based superalloy, Acta Mater. 74 (2014) 110–124, https://doi.org/10.1016/j.actamat.2014.04.039.
- [76] S. Birosca, G. Liu, R. Ding, J. Jiang, T. Simm, C. Deen, M. Whittaker, The dislocation behaviour and GND development in a nickel based superalloy during creep, Int. J. Plast. 118 (2019) 252–268, https://doi.org/10.1016/j. iiplas.2019.02.015.
- [77] F.P.E. Dunne, D. Rugg, On the mechanisms of fatigue facet nucleation in titanium alloys, Fatigue Fract. Eng. Mater. Struct. 31 (2008) 949–958, https://doi.org/ 10.1111/j.1460-2695.2008.01284.x.
- [78] C. Ribart, A. King, W. Ludwig, J.P.C. Bertoldo, H. Proudhon, In situ synchrotron X-ray multimodal experiment to study polycrystal plasticity, J. Synchrotron Radiat. 30 (2023) 379–389, https://doi.org/10.1107/S1600577522011705.
- [79] L. Renversade, R. Quey, W. Ludwig, D. Menasche, S. Maddali, R.M. Suter, A. Borbély, Comparison between diffraction contrast tomography and high-energy diffraction microscopy on a slightly deformed aluminium alloy, IUCrJ 3 (2016) 32–42, https://doi.org/10.1107/S2052252515019995.

- [80] H.F. Poulsen, S.F. Nielsen, E.M. Lauridsen, S. Schmidt, R.M. Suter, U. Lienert, L. Margulies, T. Lorentzen, D. Juul Jensen, Three-dimensional maps of grain boundaries and the stress state of individual grains in polycrystals and powders, J. Appl. Crystallogr. 34 (2001) 751–756, https://doi.org/10.1107/ S0021889801014273.
- [81] J.V. Bernier, R.M. Suter, A.D. Rollett, J.D. Almer, High-energy X-ray diffraction microscopy in materials science, Annu. Rev. Mater. Res. 50 (2020) 395–436, https://doi.org/10.1146/annurev-matsci-070616-124125.
- [82] Y. Hayashi, D. Setoyama, Y. Hirose, T. Yoshida, H. Kimura, Intragranular three-dimensional stress tensor fields in plastically deformed polycrystals, Science 366 (2019) 1492–1496, https://doi.org/10.1126/science.aax9167.
- [83] Y. Hayashi, Y. Hirose, Y. Seno, Polycrystal orientation mapping using scanning three-dimensional X-ray diffraction microscopy, J. Appl. Crystallogr. 48 (2015) 1094–1101. https://doi.org/10.1107/51600576715009899.
- 1094–1101, https://doi.org/10.1107/S1600576715009899.

  [84] N.A. Henningsson, S.A. Hall, J.P. Wright, J. Hektor, Reconstructing intragranular strain fields in polycrystalline materials from scanning 3DXRD data, J. Appl. Crystallogr. 53 (2020) 314–325, https://doi.org/10.1107/S1600576720001016.
- [85] J. Hektor, S.A. Hall, N.A. Henningsson, J. Engqvist, M. Ristinmaa, F. Lenrick, J. P. Wright, Scanning 3DXRD measurement of grain growth, stress, and formation of Cu6Sn5 around a tin whisker during heat treatment, Materials 12 (2019) 446, https://doi.org/10.3390/ma12030446.